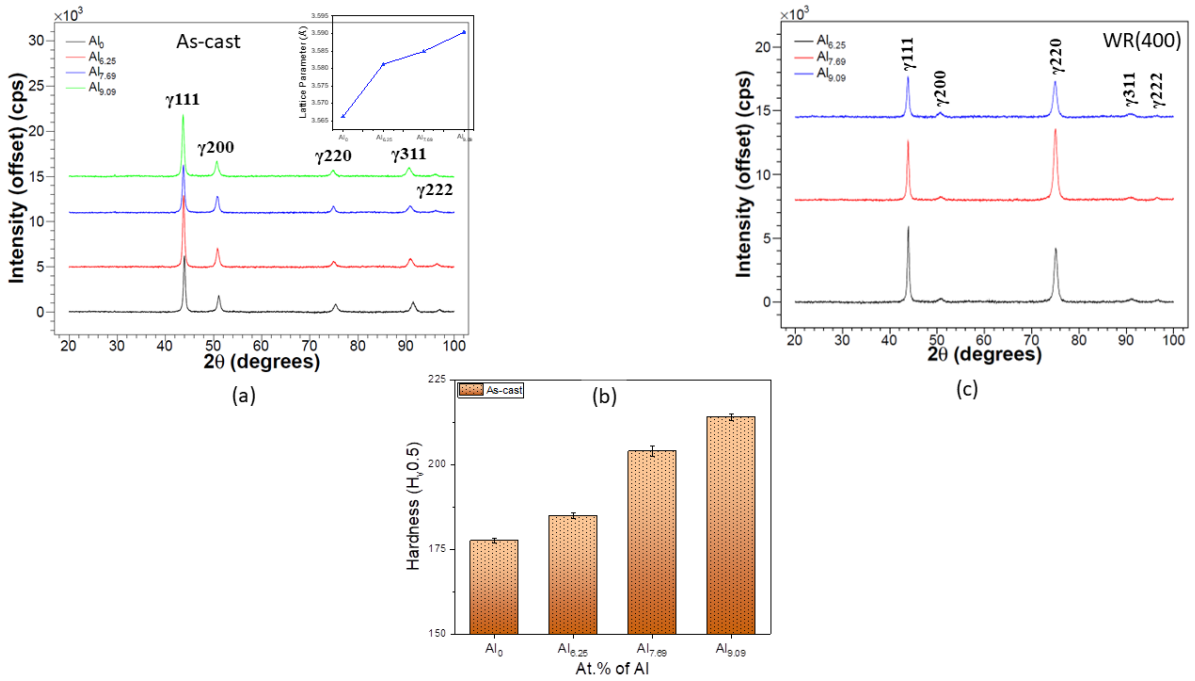

Fig. 1: (a) XRD patterns and (b) Hardness profile of as-cast AlxCoCrNi MEAs. Variations of lattice parameters with variations of Al-content are shown in the inset of (a). (c) XRD patterns of 85% warm-rolled AlxCoCrNi MEAs.

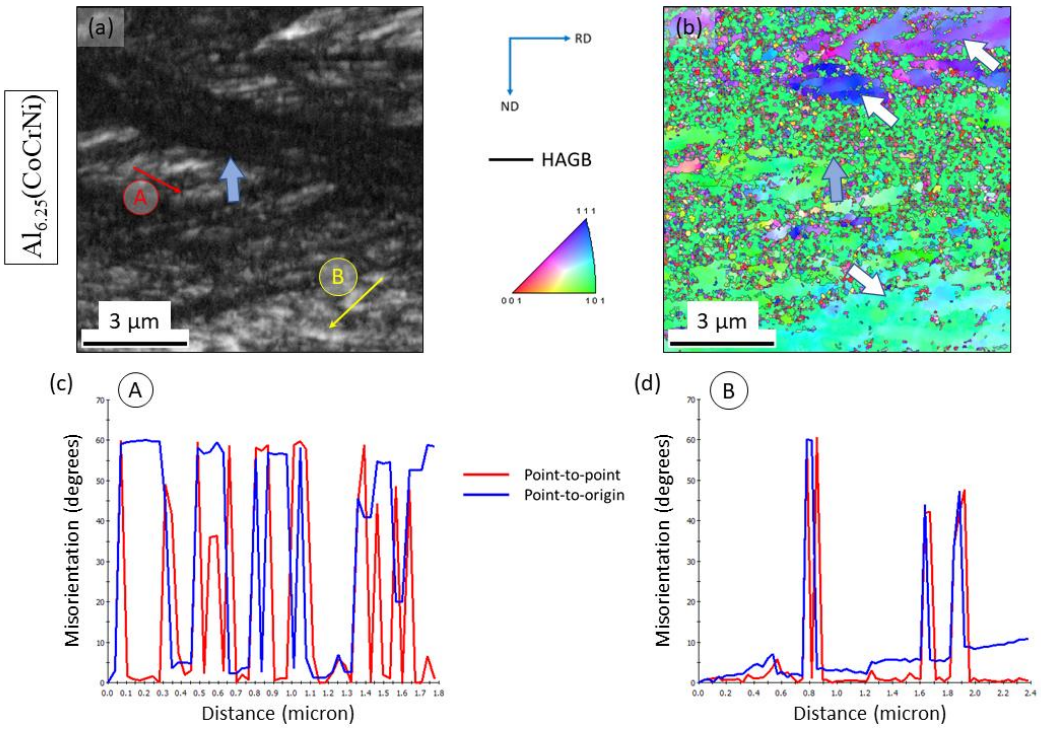

Fig. 2: (a) IQ map and (b) IPF map of $Al_{6.25}$(CoCrNi) MEA after 85% warm-rolling. (c) and (d) are misorientation profiles of locations A and B, respectively, mentioned in (a).

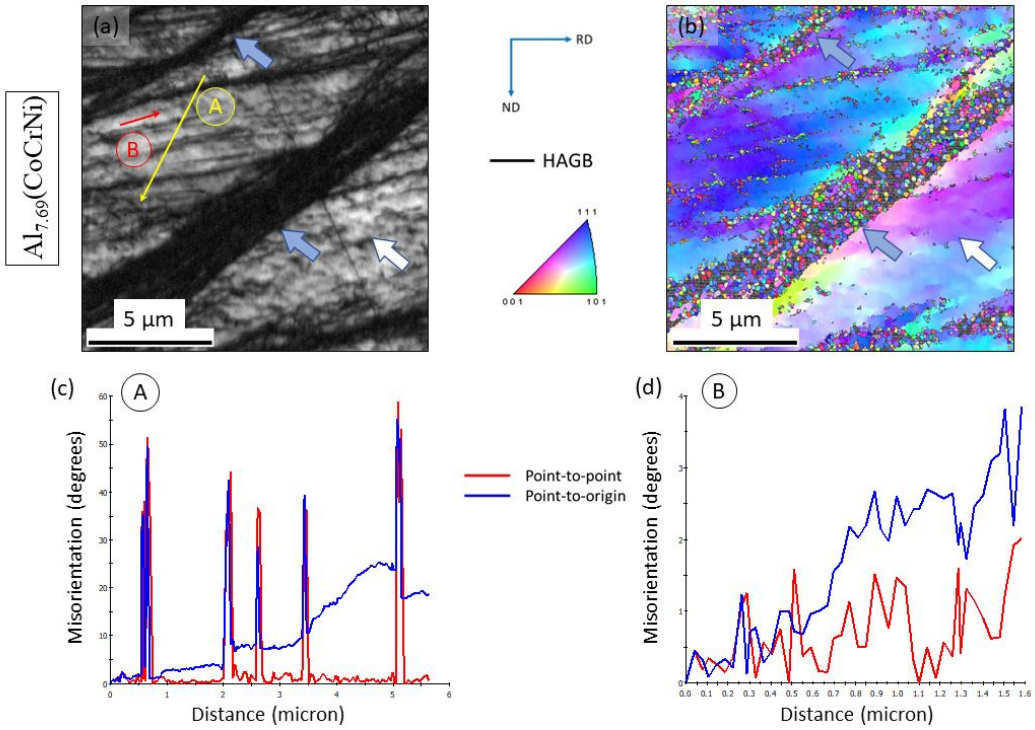

Fig. 3: (a) IQ map and (b) IPF map of $Al_{7.69}$(CoCrNi) MEA after 85% warm-rolling. (c) and (d) are misorientation profiles of locations A and B, respectively, mentioned in (a).

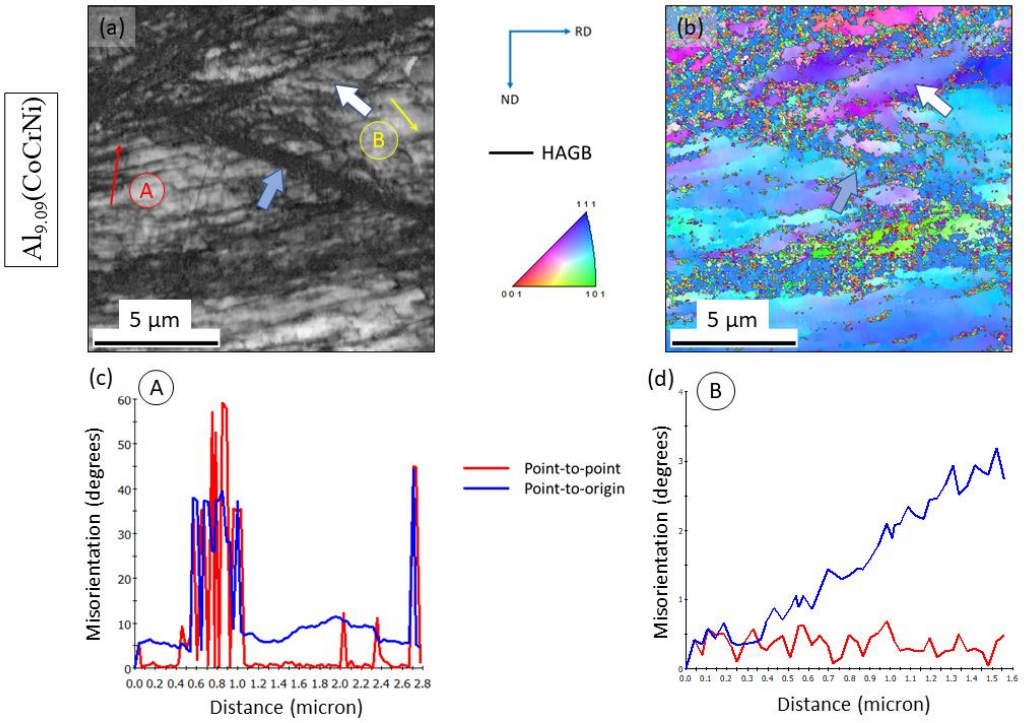

Fig. 4: (a) IQ map and (b) IPF map of $Al_{9.09}$(CoCrNi) MEA after 85% warm-rolling. (c) and (d) are misorientation profiles of locations A and B, respectively, mentioned in (a).

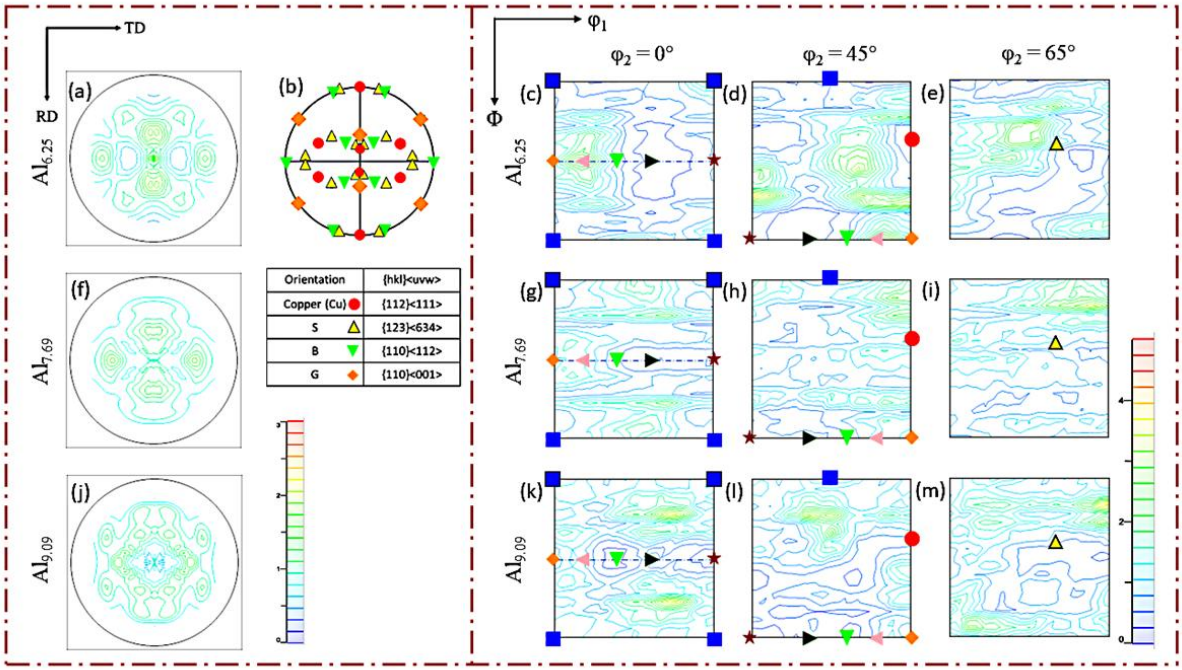

Fig. 5: (111) PFs of $Al_{6.25}$ (a), $Al_{7.69}$ (f), and $Al_{9.09}$ (j) MEAs after 85% warm-rolling. (d) shows the ideal (111) PF with the important deformation texture components of FCC materials. Selected ODF sections at φ2 = 0° (c, g, k), 45° (d, h, l), and 65° (e, i, m) of $Al_{6.25}$ (c-e), $Al_{7.69}$ (g-i), and $Al_{9.09}$ (k-m) MEAs after 85% warm-rolling.

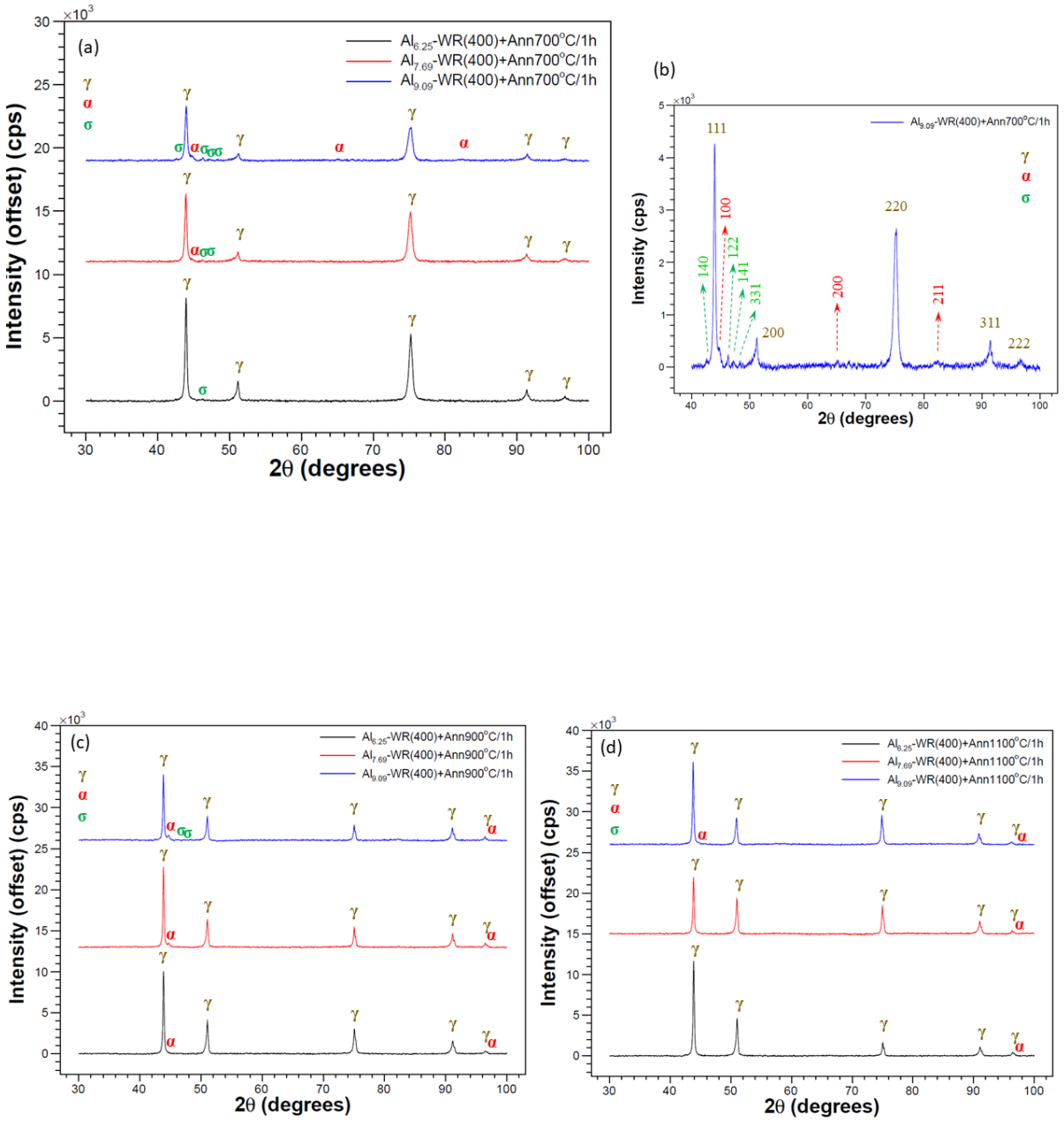

Fig. 6: XRD patterns of $Al_xCoCrNi$ MEAs after annealing at 700 °C (a), 900 °C (c) and 1100 °C (d). (b) shows detailed XRD profile of $Al_{9.09}$(CoCrNi) MEA after annealing at 700 °C.

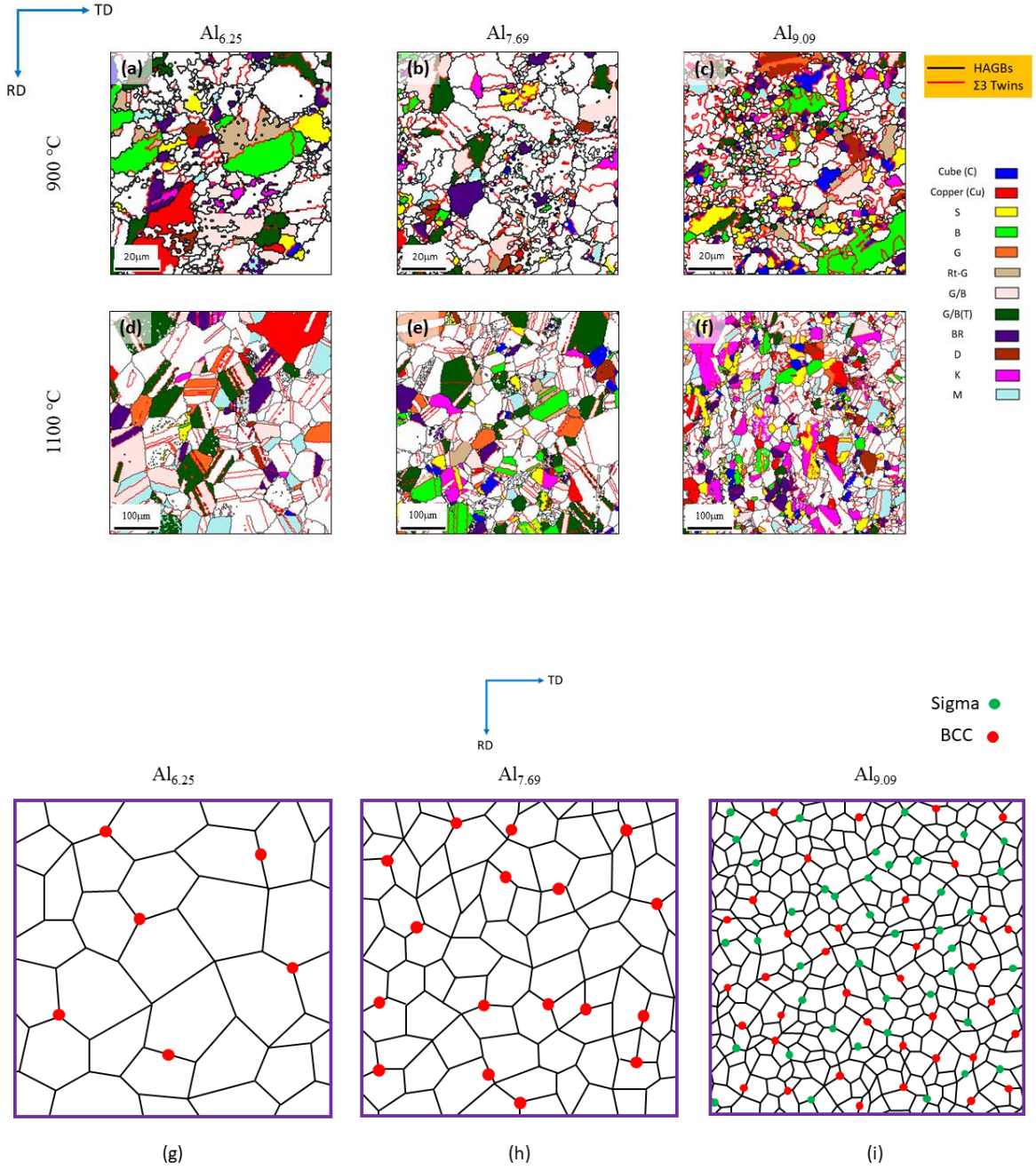

Fig. 7: OMs of $Al_{6.25}$ (a, d) $Al_{7.69}$ (b, e) and $Al_{9.09}$ (c, f) MEAs after annealing at 900 °C (a-c) and 1100 °C (d-f). Schematic diagrams are presented for 900 °C annealed $Al_{6.25}$ (g) $Al_{7.69}$ (h) and $Al_{9.09}$ (i) MEAs.

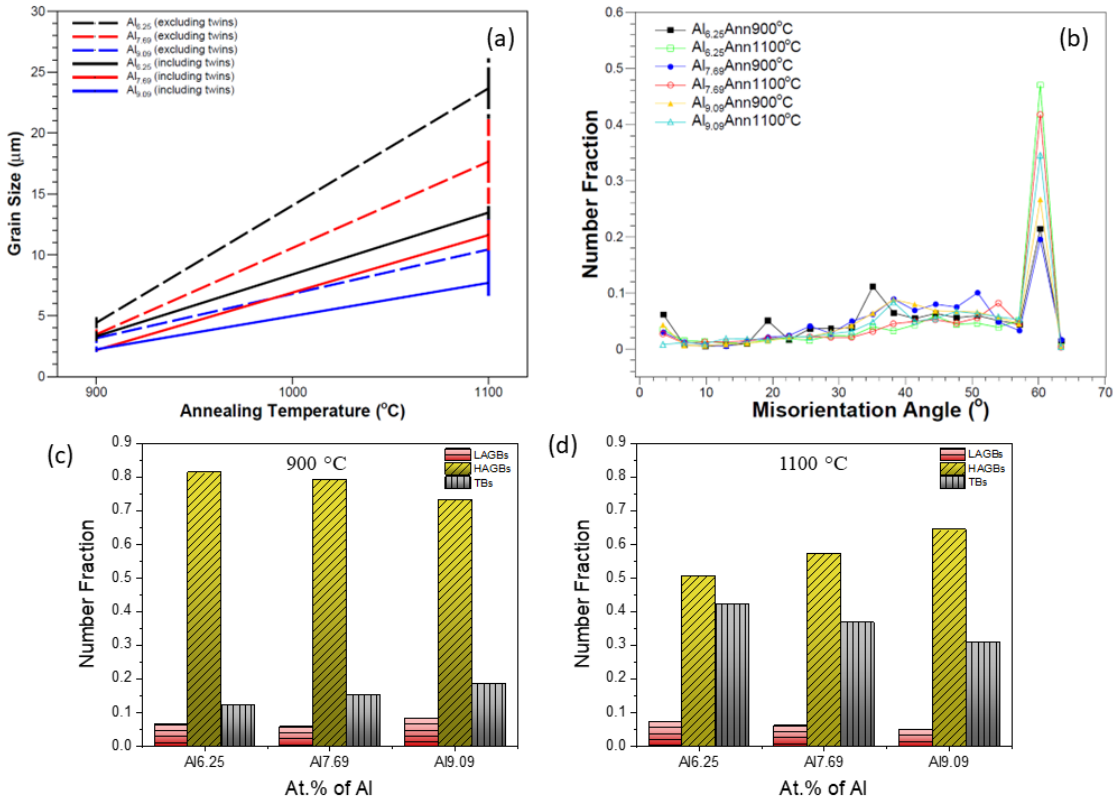

Fig. 8: (a) Variation of grain size with annealing temperature. (b) Misorientation angle distribution of annealed Al-content MEAs. Grain boundary characteristics distribution (GBCD) of (c) 900 °C and (d) 1100 °C annealed Al-content MEAs.

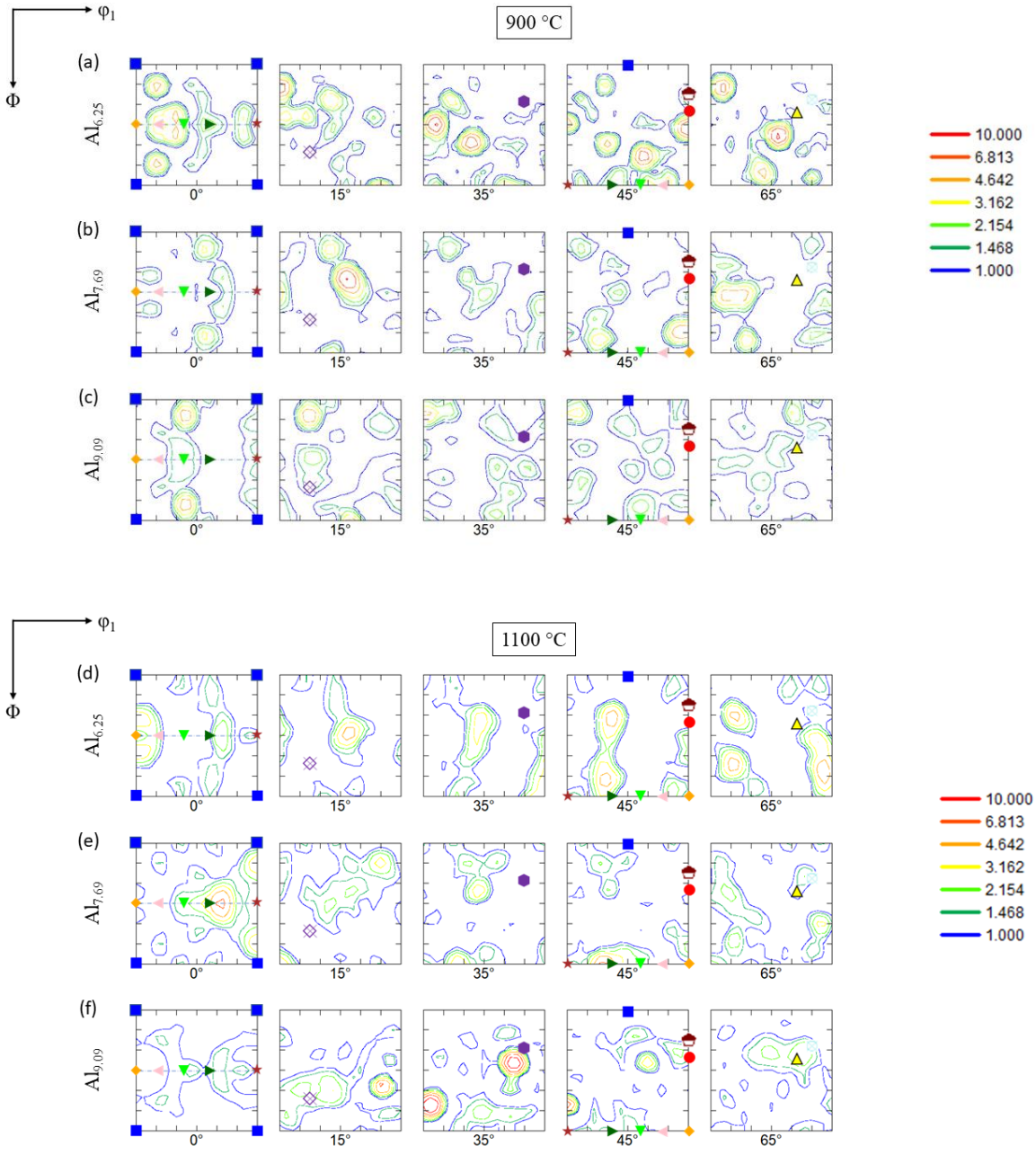

Fig. 9: Selected ODF sections of $Al_{6.25}$ (a, d) $Al_{7.69}$ (b, e) and $Al_{9.09}$ (c, f) MEAs after annealing at 900 °C (a-c) and 1100 °C (d-f). The legends are shown in Table 2.

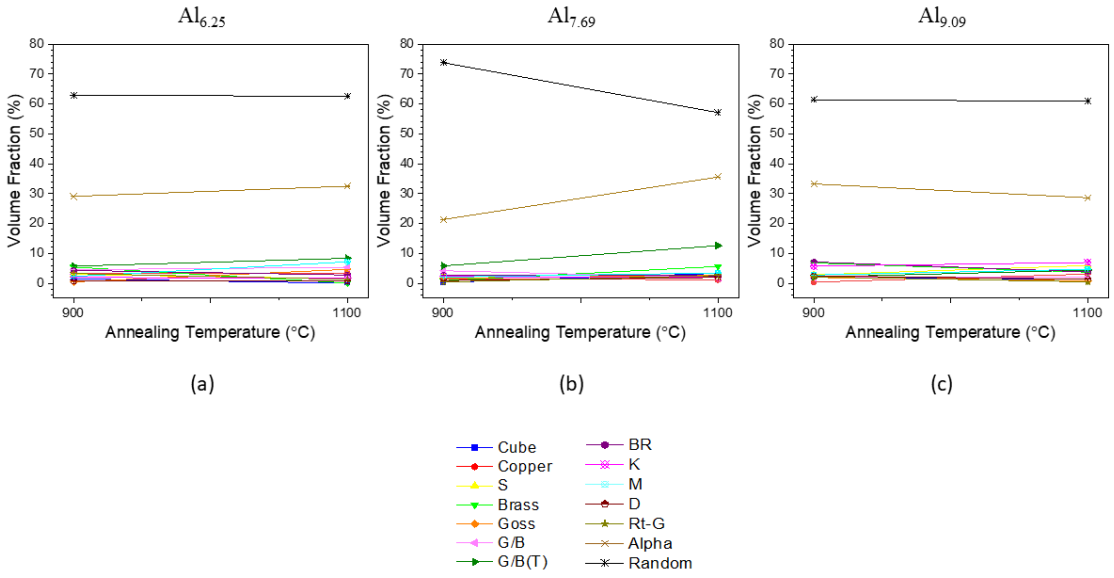

Fig. 10: Variation of volume fraction of different texture components with annealing temperatures for $Al_{6.25}$ (a), $Al_{7.69}$ (b), and $Al_{9.09}$ (c) MEAs.

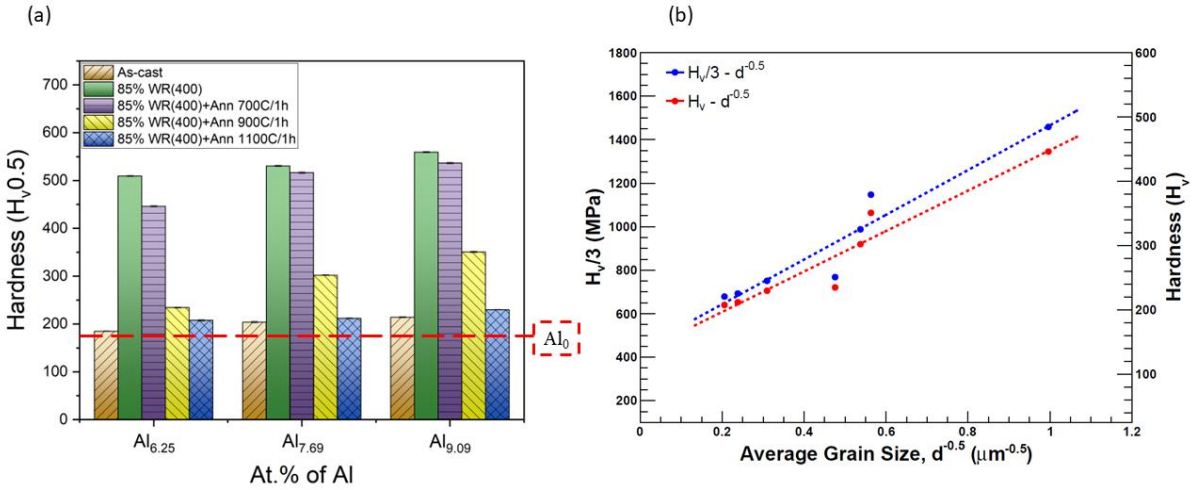

Fig. 11: (a) Hardness profile of as-cast, deformed, and annealed $Al_xCoCrNi$ MEAs. The red dashed line indicates the hardness of as-cast CoCrNi MEA (Al_0). (b) Hall-Petch relationship of $Al_xCoCrNi$ MEAs constructed using hardness (H_v, red line) and yield strength ($H_v/3$, blue line).

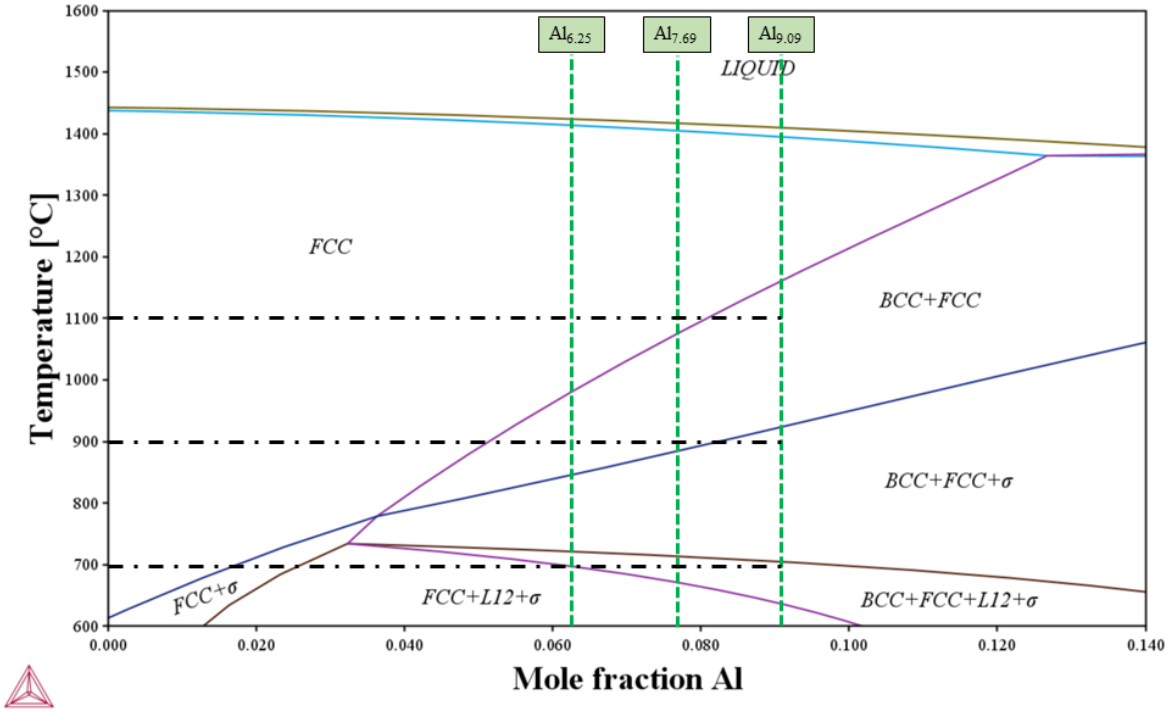

Fig.12: Phase diagram of $Al_xCoCrNi$ MEAs constructed using ThermoCalc software.

Table 1: Compositions of as-cast $Al_xCoCrNi$ MEAs obtained from EDS analysis.

Sample No.		**Al**	**Co**	**Cr**	**Ni**
Al_0	Nominal	-	33.33	33.33	33.33
	Experimental	-	33.50 ± 0.34	33.64 ± 0.34	32.87 ± 0.05
$Al_{6.25}$	Nominal	6.25	31.25	31.25	31.25
	Experimental	5.30 ± 0.21	32.60 ± 0.18	30.88 ± 0.40	31.22 ± 0.06
$Al_{7.69}$	Nominal	7.69	30.77	30.77	30.77
	Experimental	6.68 ± 0.27	32.25 ± 0.07	30.07 ± 0.50	31.00 ± 0.25
$Al_{9.09}$	Nominal	9.09	30.3	30.3	30.31
	Experimental	7.99 ± 0.16	31.64 ± 0.06	29.75 ± 0.31	30.62 ± 0.20

(All values are in atomic %)

Table 2: Key deformation and recrystallization texture components in warm-rolled FCC phase.

Orientation	{hkl}<uvw>	Euler angles (°)	Symbols
		(ϕ_1,Φ,ϕ_2)	
Cube (C)	{001}<100>	0, 0, 0	
Copper (Cu)	{112}<111>	90, 35, 45	
S	{123}<634>	59, 37, 63	
B	{110}<112>	35, 45, 0	
G	{110}<001>	0, 45, 0	
Rt-G	{110}<110>	90, 45, 0	
G/B	{110}<115>	17, 45, 0	
G/B(T)	{110}<111>	55,45,0	
BR	{236}<385>	80, 31, 34	
D	{113}<332>	90,27,45	
K	{142}<211>	27,64,15	
M	{13 6 25}<20 15 14>	80, 30, 65	

Highlights

- Effect of Al on warm-rolling and annealing of the CoCrNi medium entropy alloys
- Development of ultrafine microstructure with the presence of dense shear bands during deformation
- Weak brass-type deformation texture irrespective of the Al-concentration
- Finer grains for higher Al-concentrated MEA, irrespective of annealing temperature
- Weak recrystallization texture and development of BCC and sigma-phase on annealing

Evolution of Microstructure and Texture in Al-containing CoCrNi Medium entropy alloys during Severe Warm-rolling

J. Saha[a,*], P.V. Cobbinah[a], T. Hiroto[b], S. Matsunaga[a], Y. Toda[b], Y.Yamabe-Mitarai[a]

[a] Department of Advanced Materials Science, The University of Tokyo, 5-1-5. Kashiwanoha, Kashiwa, Chiba 272-8561, Japan

[b] National Institute for Materials Science, 1-2-1, Sengen, Tsukuba, Ibaraki 305-0047, Japan

Abstract

Al, as an alloying element, can influence the properties of the single-phase equiatomic CoCrNi MEA. In this study, different alloys of different Al concentrations added to CoCrNi MEA ($Al_xCoCrNi$) were prepared by warm rolling to understand the effect of Al. The alloys were warm-rolled at 400 °C up to an 85% thickness reduction, followed by isochronal annealing at 700 – 1100 °C. The microstructure after deformation reveals the development of deformation heterogeneities such as shear bands and deformation nano-twins. The evolution of the weak brass component is seen after deformation. Different phases, such as BCC and sigma, evolve upon annealing treatment at different temperatures. The higher Al-content MEA ($Al_{9.09}$) shows comparatively finer recrystallized microstructure irrespective of the annealing temperatures. Also, weak recrystallization texture develops after annealing, and the deformation texture components lying on α-fiber are preserved. This indicates the absence of preferential nucleation and growth during annealing. The hardness in the as-cast, deformed, and annealed conditions increases with increasing Al content, indicating the influence of Al in the strengthening of the $Al_xCoCrNi$ MEAs.

Keywords: Medium entropy alloys; Al-addition; Thermo-mechanical treatment; Microstructure and texture; Mechanical properties

1. Introduction

With a nod to modernism and in step with the times, in the early 2000s, a new and novel alloy design approach unlocked the concept of a larger compositional space of materials by overcoming the barrier of the conventional one-principal-element alloy design concept. This new category of materials has been named High entropy alloys (HEAs) or Complex concentrated alloys (CCAs) [1, 2]. Although HEAs contain a large number of elements, it has been well-established that most of these alloys can still exhibit solid solution phases, such as the face-centered cubic (FCC) [2], body-centered cubic (BCC) [1], hexagonal closed-packed (HCP) [3-6], or the mixture of FCC and BCC [7, 8], instead of forming intermetallic phases. HEAs form simple solid solution phases due to the higher configuration entropy (ΔS_{conf}), which minimizes the free energy sufficiently to stabilize the phases with simple crystal structures [1, 2]. The HEAs ($\Delta S_{conf} \geq 1.5R$) [9-20] and Medium entropy alloys (MEAs, $1.5R < \Delta S_{conf} \leq 1R$, R is the universal gas constant) always interest researchers because of their fascinating features. Nevertheless, it took the MEAs considerably longer to become well-known. CoCrNi, one of such MEAs, attracts attention due to its distinctive facets, such as its low stacking fault energy, formation of extensive deformation nano-twins, and FCC to HCP phase transformation [21-26]. In addition, the exceptional mechanical properties [21, 22, 27, 28] of CoCrNi MEA have led to in-depth studies. Studies on the thermo-mechanical behavior of CoCrNi are thus imperative to understanding the tailoring of microstructure and enhancement of mechanical properties [29-33].

Severe lattice distortion is one of the four core effects of HEAs. Owing to the multiple principal elements composing these multicomponent alloy systems, there is a possibility of an atomic size mismatch of the elements. The atomic size mismatch of the elements leads to the distortion of the unit cell. The severe unit cell distortion affects the mechanical properties of the alloys by preventing dislocation motion.

When added to the FCC single-phase CoCrFeMnNi HEA, Al can introduce the BCC phase to the alloy system [34, 35]. Several studies on Al-containing HEAs suggest mechanical properties improve with increasing the Al content [36-38]. The addition of Al is primarily responsible for the substantial solid solution strengthening of the alloy due to its significantly larger atomic radius among the constituent elements, Co, Cr, Fe, Cu, or Ni. Combining with Fe, Co, and Ni, Al has a greater propensity for forming the BCC phase, which leads to strength enhancement than the single-phase FCC HEAs. Similarly, the introduction of Al to the CoCrNi MEA improves mechanical properties by also forming BCC or other phases [39-43]. Many of these studies observed that Al content beyond ~11 at.% produces the BCC phase along with the FCC matrix [39, 41, 43], while the sigma (σ) phase develops once Al content reaches ~25 at.% [39]. Furthermore, the effect of cold-rolling on Al-containing CoCrNi MEAs has been investigated by a few researchers. These studies revealed the development of cracks in samples with higher Al content (> ~10 at.%) during severe cold-rolling [39].

On the other hand, the warm-rolling process is another attractive processing route option. Finely distributed grains of the FCC matrix and enhanced mechanical properties during the warm-rolling followed by annealing of CoCrNi MEA make this route more attractive for the CoCrNi MEA [31-33]. Additionally, the lesser flow stress and superior surface finish compared to cold- and hot-rolling, respectively, make warm-rolling more worthwhile. However, the effect of warm-rolling on microstructure and texture evolution and the mechanical properties of Al-containing CoCrNi remain unresolved. The effectiveness of warm-rolling on different HEAs has been reported [35, 44, 45], but the effect of this unique processing route on MEAs still needs to be improved. In effect, it is now essential to study the impact of the alloying elements as they are always beneficial in improving the mechanical properties. Therefore, in this study, warm deformation was carried out on a range of CoCrNi alloys with varied Al content to understand the effect of Al on tailoring the microstructure and crystallographic texture. The addition of Al can introduce different phases, and the warm-rolling process could

87 further improve the mechanical properties. The observations described here are believed to be
88 very effective for future studies on this deformation process.

89 **2. Experimental Procedure**

90 *2.1 Sample Processing*

91 The MEAs with different compositions (Al_x; x = 0, 6.25, 7.69 and 9.09 at.%) were prepared
92 by vacuum arc melting furnace in a Ti-gettered argon atmosphere using the raw materials with
93 a purity level of more than 99.9%. The cast ingots were flipped and remelted at least five times
94 to improve chemical homogeneity. To validate the distribution of the elements in the alloys,
95 Energy Dispersive Spectroscopy (EDS) was performed for each sample. Table 1 presents the
96 experimental details along with the nominal compositions of the MEAs. The ingots were
97 thermo-mechanically processed through warm-rolling at 400 °C (WR(400)) to attain a final
98 thickness reduction of ~85% using a rolling machine with a diameter of 300 mm (ONO Roll
99 & Co., Japan). To achieve the final thickness level, the warm-rolling was scheduled for the
100 multipass route. Before the first pass, the samples were kept inside the furnace at 400 °C for
101 30 minutes and 10 minutes for the subsequent passes until achieving the final thickness. All
102 the warm-rolled samples were annealed at 700 °C, 900 °C, and 1100 °C for 1 hour, followed
103 by water quenching.
104

Table 1: Compositions of as-cast $Al_xCoCrNi$ MEAs obtained from EDS analysis.

Sample No.		Al	Co	Cr	Ni
Al_0	Nominal	-	33.33	33.33	33.33
	Experimental	-	33.50 ± 0.34	33.64 ± 0.34	32.87 ± 0.05
$Al_{6.25}$	Nominal	6.25	31.25	31.25	31.25
	Experimental	5.30 ± 0.21	32.60 ± 0.18	30.88 ± 0.40	31.22 ± 0.06
$Al_{7.69}$	Nominal	7.69	30.77	30.77	30.77
	Experimental	6.68 ± 0.27	32.25 ± 0.07	30.07 ± 0.50	31.00 ± 0.25
$Al_{9.09}$	Nominal	9.09	30.3	30.3	30.31
	Experimental	7.99 ± 0.16	31.64 ± 0.06	29.75 ± 0.31	30.62 ± 0.20

(All values are in atomic %)

2.2 Characterization

To identify the phases and determine the crystal structure of the alloys, X-ray Diffraction (XRD; SmartLab, Rigaku, Japan) was conducted for all the deformed and annealed samples using Cu-K_α radiation (λ = 1.5418Å), operated at 40kV and 30mA. All the measurements were performed with a constant step size and a scan rate of 0.02° and 2° /min, respectively, for each sample in the 2θ range of 20° to 100°.

The microstructure and microtexture of the alloys were investigated using JSM-7200F Field Emission Gun Scanning Electron Microscope (FEG-SEM; JEOL, Japan) equipped with an EDAX Electron Backscatter Diffraction (EBSD) system (EDAX-AMETEK inc., USA). A very systematic polishing schedule was maintained to prepare the samples suitable for the EBSD technique, starting with mechanical polishing using emery papers and diamond suspensions of 9 µm, 3 µm, and 1 µm, followed by the final step of fine colloidal silica suspension. The scan rate was kept constant at 0.04 µm (40 nm) for all deformed samples and varied between 0.6 µm (600 nm) and 1.75 µm (1750 nm) for the samples annealed at 900 °C and 1100 °C. The elemental distribution of the alloys was studied using the EDAX EDS system (EDAX-AMETEK Inc., USA), integrated with SEM. Several EBSD scans were performed at different

123 locations of the deformed and annealed samples for microstructure and microtexture analysis
124 of the alloys. To measure the microtexture, the scans were merged and analyzed in TSL-
125 OIMTM software of version 7.0 (EDAX-AMETEK Inc., USA). The orientation distribution
126 functions (ODFs) and (111) pole figures (PFs) were calculated using the parameters of
127 orthotropic symmetry and harmonic series expansion method with the Series Rank of 22 from
128 the merged scans of each sample. The Bunge notations with the Euler angles of the different
129 essential texture components, which were used to construct the ODF sections, are tabulated in
130 Table 2.

131 Textures of the deformed samples were further investigated by the bulk-texture
132 measurements using XRD (SmartLab, Rigaku, Japan) with a Cu-K_α source (λ = 1.5418Å),
133 equipped with an alpha (α) - beta (β) sample stage and operated at 45kV and 200mA, to
134 comprehend the textures in a broader area. The X-ray bulk-texture measurements were taken
135 from the rolling plane section (bounded by rolling direction (RD) and transverse direction
136 (TD)) of the specimens. For this purpose, the samples with the dimensions of 10 mm X 15 mm
137 were extracted from the deformed materials and mechanically polished using emery papers and
138 different grades of diamond suspension as the final polishing steps. The (111), (200), and (220)
139 pole figures (PFs) were measured with the step sizes of α and β being 3° and the scan rate of
140 150 °/min. The PFs and (orientation distribution function) ODF maps were visualized and
141 calculated by SmartLab Studio II (Rigaku) software. The reconstruction of the ODF maps from
142 measured PFs was carried out using the direct numerical calculation method of the WIMV
143 model.

144 The mechanical properties of the as-cast, deformed, and annealed samples were studied by
145 Vickers microhardness testing (HMV, Shimadzu Corporation, Japan). The microhardness
146 testing was performed on the rolling surface of each sample with the combination of 500 gm-f
147 load and 15 seconds of dwell time. The mean of a minimum of 15 hardness measurements was
148 reported with the standard error for every sample.

3. Results

3.1 Phase identification, crystal structure, and mechanical properties of as-cast samples

Fig. 1 describes the phases present in the as-cast samples of the $Al_xCoCrNi$ MEAs through the XRD profiles. The XRD profiles in Fig. 1(a) show the single FCC crystalline structure as the main phase in the as-cast CoCrNi MEA. Moreover, the XRD profiles of the $Al_xCoCrNi$ MEAs indicate no change in the crystal structure of the alloys even after 9.09 at.% Al addition. We surmise that the primary cause of the strong 111 peak is due to the orientation of the columnar grains in that direction. However, the peaks of the $Al_xCoCrNi$ MEAs shift towards the lower 2θ values compared to the CoCrNi MEA. This observation confirms that Al plays a significant role in the lattice distortion of CoCrNi MEAs due to the larger atomic radius of Al compared to other constituents (r_{Al} = 1.4317Å, r_{Co} = 1.251Å, r_{Cr} = 1.2491Å and r_{Ni} = 1.2459Å) [15]. The change in lattice parameter can be observed in the inset of Fig. 1(a), which shows the lattice parameter of $Al_xCoCrNi$ MEA increased with the addition of Al. The lattice parameter of CoCrNi MEA is 3.566Å, which changes to 3.59Å after Al addition of 9.09 at.%.

Although the XRD profiles show no precipitates, the increase of the solid solution strengthening due to the lattice distortion could be identified from the microhardness profile of the as-cast samples (Fig. 1(b)). The as-cast CoCrNi MEA (Al_0) shows a hardness of ~178 H_v, while there is a sharp increase in the hardness values with the increase of the Al content. The hardness of the $Al_{9.09}$ containing MEA increases by ~37% (~214 H_v) compared to Al_0 MEA.

3.2 Analysis of phase identification, microstructure, and grain orientation after deformation

The XRD profiles of the 85% warm-rolled Al_x-MEA specimens, displayed in Fig. 1(c), suggest no phase evolution during the deformation process, indicating the stability of the FCC phase even at higher deformation temperatures. Fig. 2 describes the microstructure of $Al_{6.25}$ MEA after 85% WR(400). After severe deformation, the microstructure exhibits an elongated

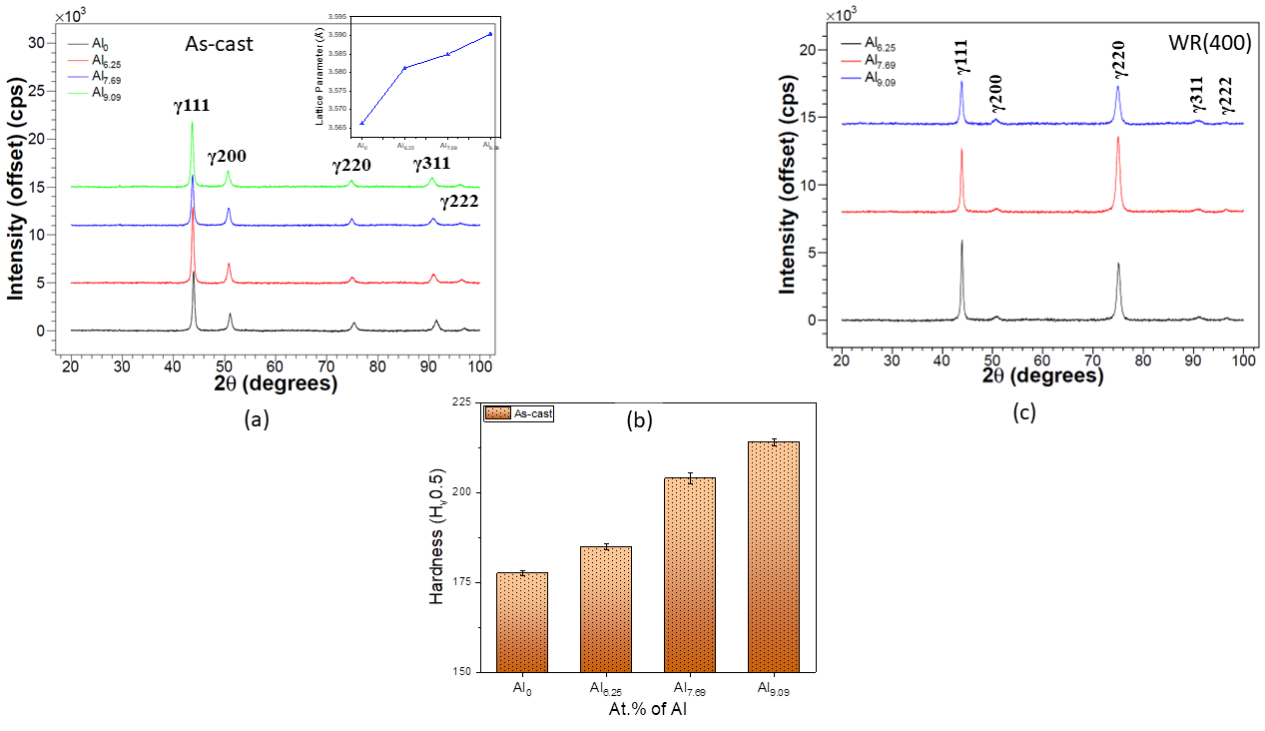

Fig. 1: (a) XRD patterns and (b) Hardness profile of as-cast $Al_xCoCrNi$ MEAs. Variations of lattice parameters with variations of Al-content are shown in the inset of (a). (c) XRD patterns of 85% warm-rolled $Al_xCoCrNi$ MEAs.

lamellar banded structure along the rolling direction (RD) as shown in Fig. 2(a) (image quality (IQ) map). An extensively dense shear band (blue arrow) can be noticed to cut the grains at ~45° along the RD. Minor changes in the misorientation confirm the presence of the inclined but small lamellar banded features (white arrows) from the inverse pole figure (IPF) map (Fig. 2(b)). The misorientation profiles are drawn for the 'A' (red arrow) and 'B' (yellow arrow) locations. Location 'A' (Fig. 2(c)) shows extensive deformation revealed as significant spikes with a misorientation angle of ~60°, indicating the presence of deformation nano-twins. However, location 'B' (Fig. 2(d)) implies homogeneous deformation with the presence of very few nano-twins. Therefore, from the misorientation profiles of locations 'A' and 'B', it can be inferred that deformation occurred by twinning and slipping.

Fig. 3 displays the microstructure of the 85% warm-rolled (WR(400)) $Al_{7.69}$ MEA. Nearly identical features are observed in the IQ map (Fig. 3(a)) with the presence of extensive shear

bands (blue arrows) and lamellar intersecting bands (white arrows). The IPF map (Fig. 3(b)) corroborates the change in orientations for the shear bands and minor misorientations of the intersecting banded features. The misorientation profile from location 'A' (Fig. 3(c)) shows the development of nano-twins during deformation, whereas location 'B' (Fig. 3(d)) displays more homogeneous deformation, evident from the very low point-to-point and point-to-origin misorientations.

Also, the microstructure of 85% warm-rolled (WR(400)) $Al_{9.09}$ MEA shows similar features in Fig. 4, where thin shear bands (blue arrows) are present along with extended lamellar intersecting bands (white arrows) (Fig. 4(a)). These features can also be confirmed from the IPF map (Fig. 4(b)). The misorientation profiles (Fig. 4(c) and (d)) describe the deformation by slipping mechanism dominating over the twinning as it shows more homogeneous deformation.

Fig. 5 illustrates the evolution of the bulk-texture and micro-texture of the 85% deformed Al_x-MEAs by the WR(400) process through (111) pole figures (PFs) and selective orientation distribution function (ODF) sections, respectively. Important deformation and recrystallization texture components are cataloged in Table 2 to ease understanding. All the significant texture components overlap the ideal (111) PF, as depicted in Fig. 5(b). The development of bulk texture in the deformed $Al_{6.25}$ MEA (Fig. 5(a)) indicates the presence of brass components (B; {110}<112>), which could suggest the development of brass-type deformation texture. However, the orientation of B appears to be weaker than other orientations, as observed in the $\varphi_2 = 0°$ section of the ODF (Fig. 5(c)), where G/B orientation ({110}<115>) is more intense. In the $\varphi_2 = 45°$ section (Fig. 5(d)), the Cu component ({112}<111>) is completely absent, while, at $\varphi_2 = 65°$ section (Fig. 5(e)), the S component ({123}<634>) is present with weak intensity.

The (111) PF of the deformed $Al_{7.69}$ MEA (Fig. 5(f)) shows the development of weak brass-type deformation texture with the presence of weak brass orientation. This feature can be

corroborated by the $\varphi_2 = 0°$ section of the ODF (Fig. 5(g)), where the weakened B component lies over the α-fibre (ND//<110>), which extends from the G ({110}<001>) to rotated G orientation (Rt-G; {110}<110>). In the $\varphi_2 = 45°$ (Fig. 5(h)) and $\varphi_2 = 65°$ (Fig. 5(i)) sections, the Cu and S components, respectively, are present with very weak intensities.

A weak brass component manifests in a slightly different emerging (111) PF (Fig. 5(j)) in the texture evolution of the deformed $Al_{9.09}$ MEA. However, the $\varphi_2 = 0°$ section of the ODF (Fig. 5(k)) elucidates the presence of the α-fibre (ND//<110>), which extends from G to Rt-G through weak B. This observation can be confirmed from the $\varphi_2 = 45°$ section (Fig. 5(l)). Relatively very weak Cu and S components can be seen in $\varphi_2 = 45°$ (Fig. 5(l)) and $\varphi_2 = 65°$ (Fig. 5(m)) sections, respectively.

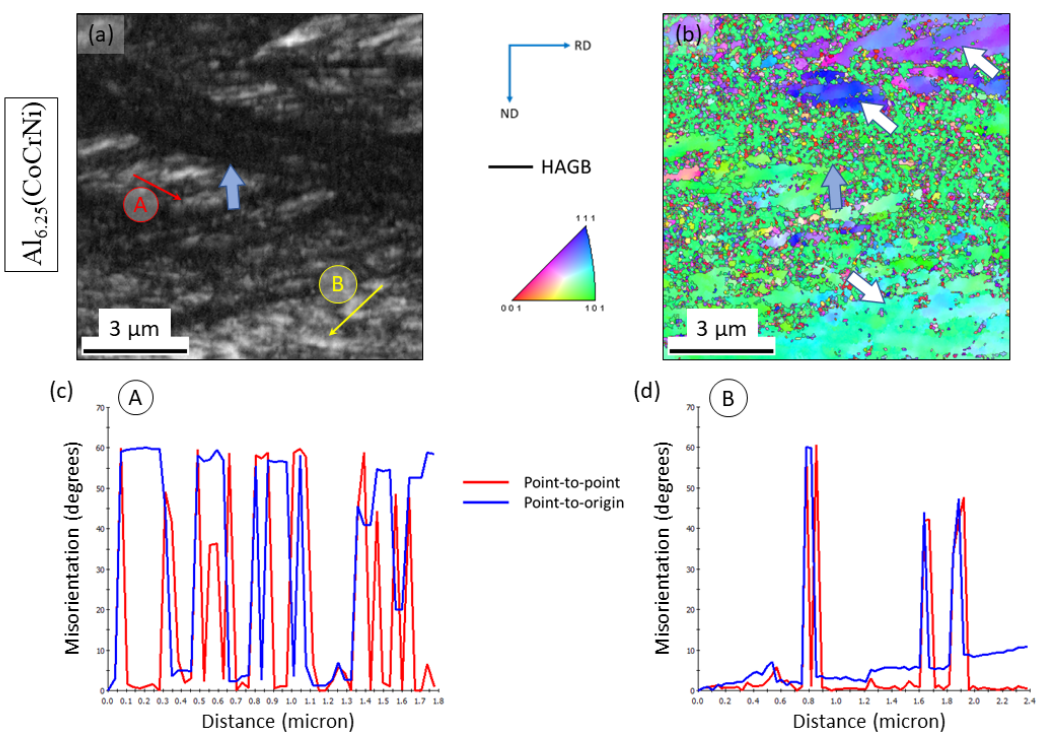

Fig. 2: (a) IQ map and (b) IPF map of $Al_{6.25}$(CoCrNi) MEA after 85% warm-rolling. (c) and (d) are misorientation profiles of locations A and B, respectively, mentioned in (a).

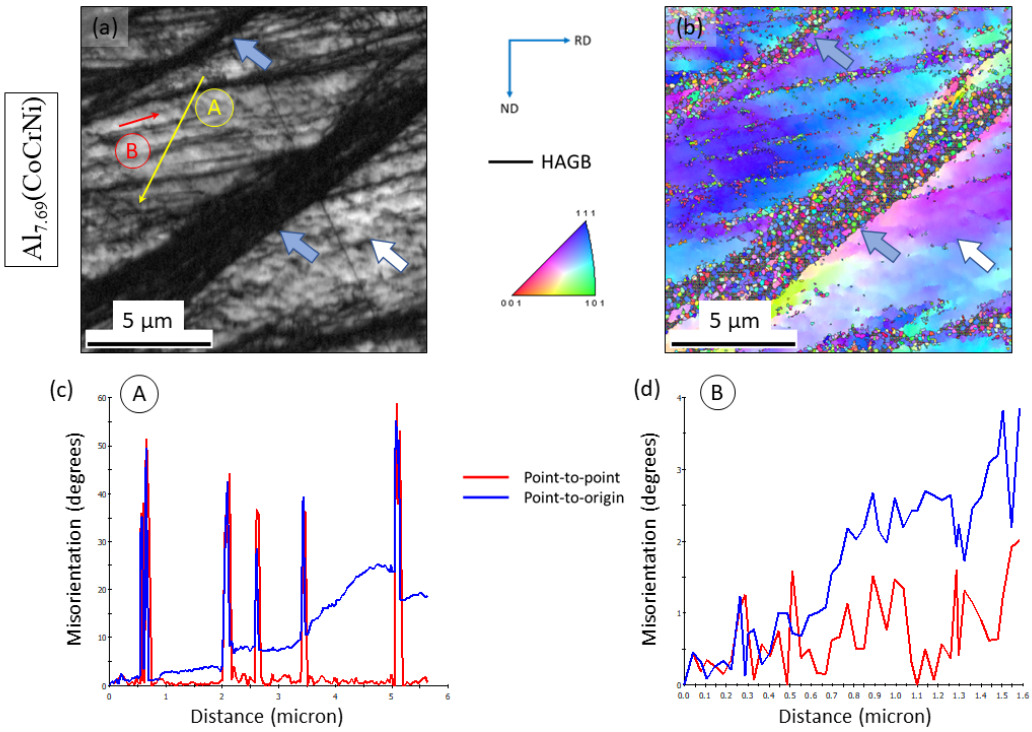

230

231 Fig. 3: (a) IQ map and (b) IPF map of $Al_{7.69}$(CoCrNi) MEA after 85% warm-rolling. (c) and
232 (d) are misorientation profiles of locations A and B, respectively, mentioned in (a).

233

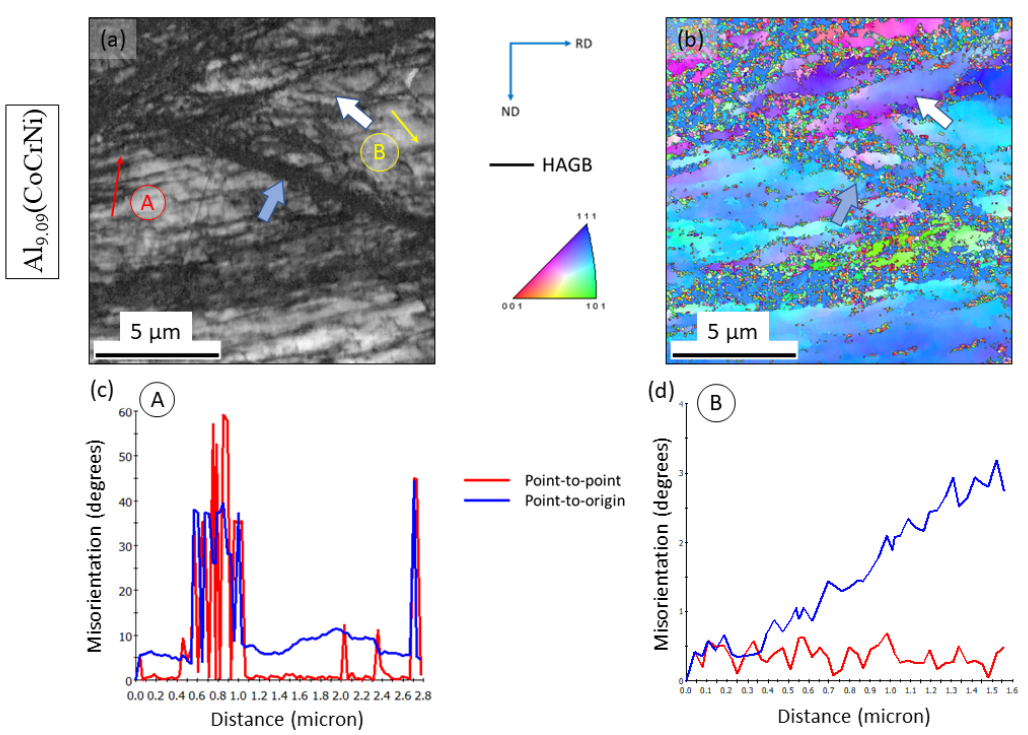

234

235 Fig. 4: (a) IQ map and (b) IPF map of $Al_{9.09}$(CoCrNi) MEA after 85% warm-rolling. (c) and
236 (d) are misorientation profiles of locations A and B, respectively, mentioned in (a).

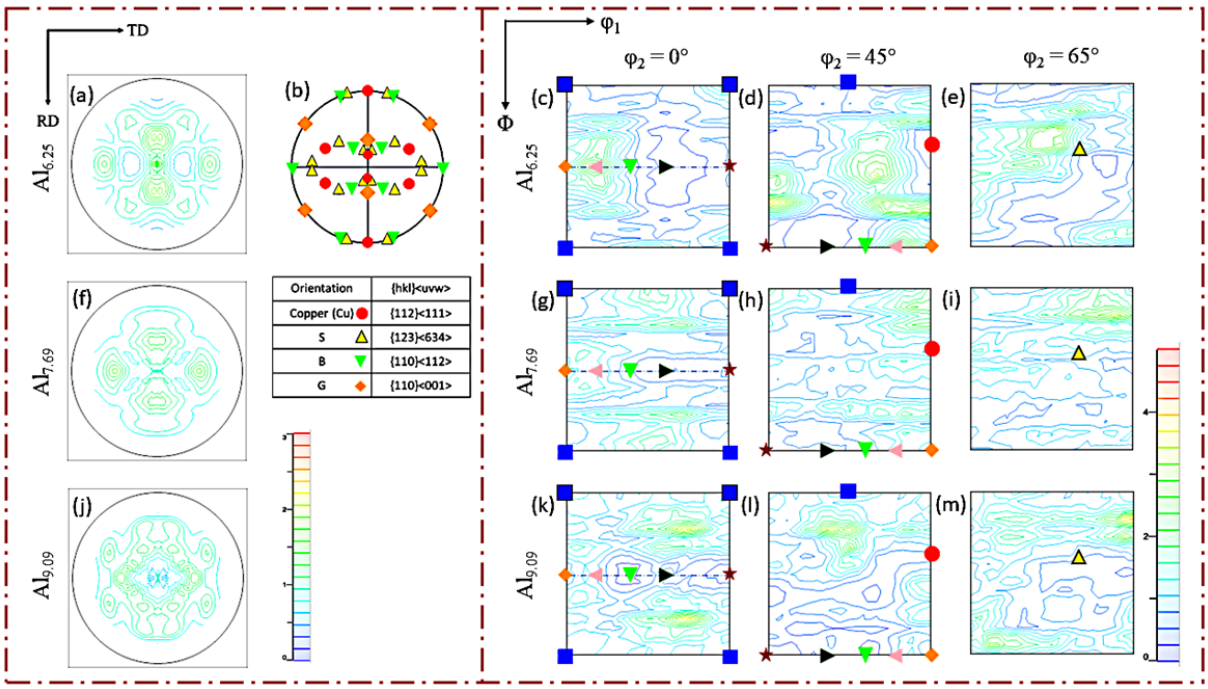

Fig. 5: (111) PFs of $Al_{6.25}$ (a) $Al_{7.69}$ (f) and $Al_{9.09}$ (j) MEAs after 85% warm-rolling. (d) shows the ideal (111) PF with the important deformation texture components of FCC materials. Selected ODF sections at φ_2 = 0° (c, g, k), 45° (d, h, l), and 65° (e, i, m) of $Al_{6.25}$ (c-e), $Al_{7.69}$ (g-i) and $Al_{9.09}$ (k-m) MEAs after 85% warm-rolling.

Table 2: Key deformation and recrystallization texture components in warm-rolled FCC phase.

Orientation	{hkl}<uvw>	Euler angles (°) (ϕ_1,Φ,ϕ_2)	Symbols
Cube (C)	{001}<100>	0, 0, 0	
Copper (Cu)	{112}<111>	90, 35, 45	
S	{123}<634>	59, 37, 63	
B	{110}<112>	35, 45, 0	
G	{110}<001>	0, 45, 0	
Rt-G	{110}<110>	90, 45, 0	
G/B	{110}<115>	17, 45, 0	
G/B(T)	{110}<111>	55,45,0	
BR	{236}<385>	80, 31, 34	
D	{113}<332>	90,27,45	
K	{142}<211>	27,64,15	
M	{13 6 25}<20 15 14>	80, 30, 65	

3.3 Phase evolution during heat treatment

To comprehend the thermal stability of the alloys during annealing at different temperatures, the XRD profiles are plotted in Fig. 6. The XRD profiles (Fig. 6(a)) for the different Al_x-MEA samples annealed at 700 °C show the development of the other phases along with stable FCC (γ) phase. The lower Al-content ($Al_{6.25}$) MEA reveals the presence of σ-phase (~46°), whereas the $Al_{7.69}$ and $Al_{9.09}$ MEAs include the BCC (α) phase and σ-phase of relatively different intensities. The $Al_{9.09}$ annealed MEA, as shown in Fig. 6(b), exhibits relatively higher intensities of the BCC and σ phases compared to the $Al_{7.69}$; however, the intensities of the FCC peaks (111 and 220) are still very strong and easily distinguishable. The lattice parameter of the BCC phase is calculated to be ~2.87Å. On the other hand, the lattice parameters of the σ-phase are ~8.79Å (a) and ~4.49Å (c), which implies the tetragonal crystal structure of the σ-phase. The formation of the BCC (α) phase can also be detected at higher annealing temperatures (900 °C (Fig. 6(c)) and 1100 °C (Fig. 6(d))). However, the samples annealed at 1100 °C show no detectable σ-phase.

3.4 Microstructure and texture evolution during recrystallization

The development of microstructures upon annealing of the severely deformed materials with different compositions is illustrated in Fig. 7. The EBSD maps, superimposed with the orientation maps (OMs) of the annealed microstructures of $Al_{6.25}$ are described in Fig. 7(a, d), $Al_{7.69}$ in Fig. 7(b, e) and $Al_{9.09}$ in Fig. 7(c, f), respectively for 900 °C and 1100 °C. Completely recrystallized and fine microstructure with grain sizes varying between ~3 – 4.5 μm (excluding annealing twins) and depending on the Al-content are observed. The presence of high-angle grain boundaries (HAGBs; marked by black lines) separates the recrystallized grains and annealing twins (TBs; red lines) upon annealing at 900 °C (Fig. 7(a-c)). Furthermore, a mixture of coarse and fine grains can be observed in the low Al-content microstructure ($Al_{6.25}$; Fig. 7(a)), whereas the microstructure is quite finer for the high Al-content sample ($Al_{9.09}$; Fig. 7(c)).

There is a discernible and typical increase in grain size at a higher annealing temperature of 1100 °C (as shown in Fig. 7(d-f)). The grain size (excluding annealing twins) ranges between ~10 – 24 μm depending on the alloy composition. Fig.7(g-i)) explains schematically the grain growth behavior.

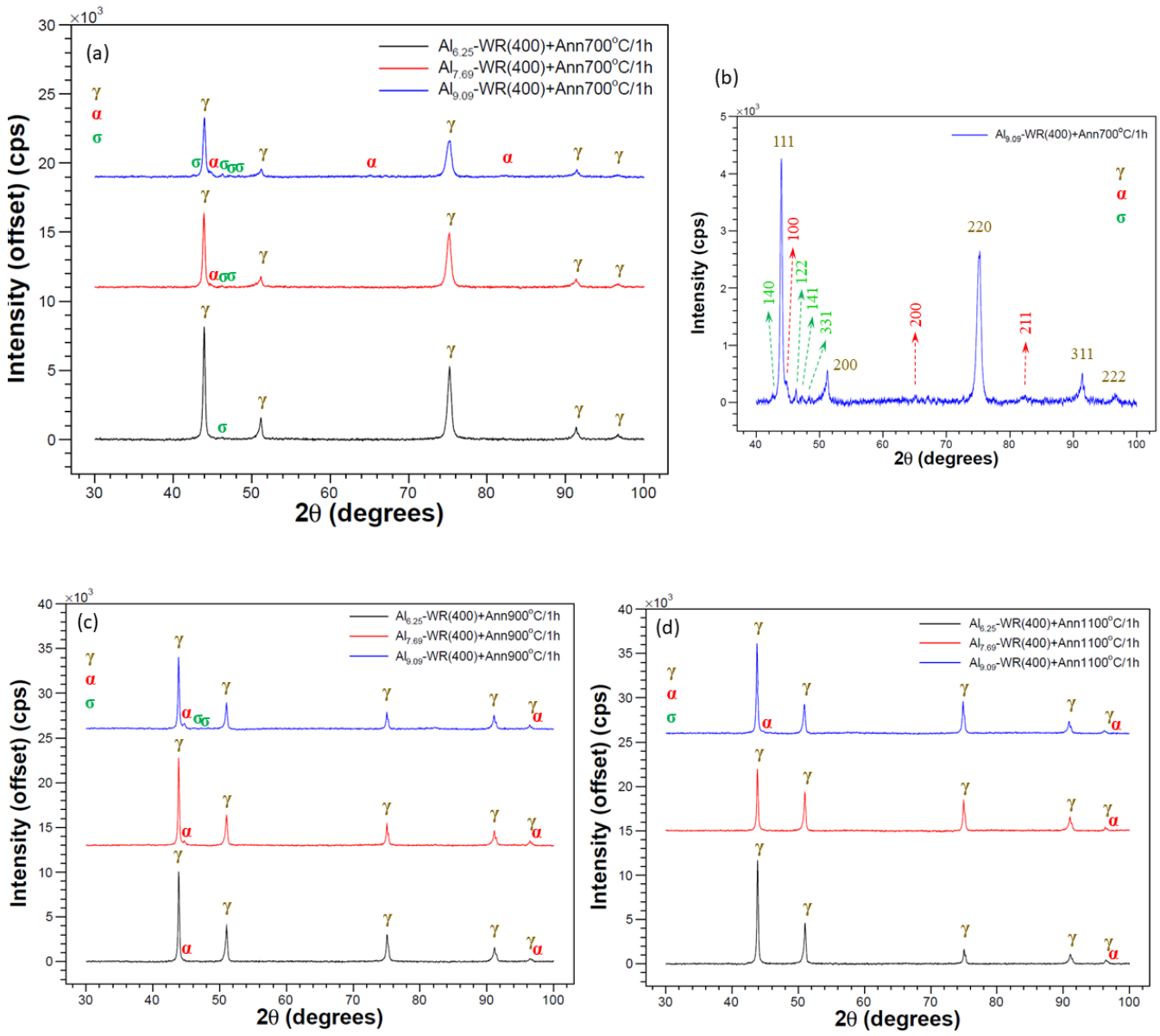

Fig. 6: XRD patterns of $Al_xCoCrNi$ MEAs after annealing at 700 °C (a), 900 °C (c) and 1100 °C (d). (b) shows detailed XRD profile of $Al_{9.09}$(CoCrNi) MEA after annealing at 700 °C.

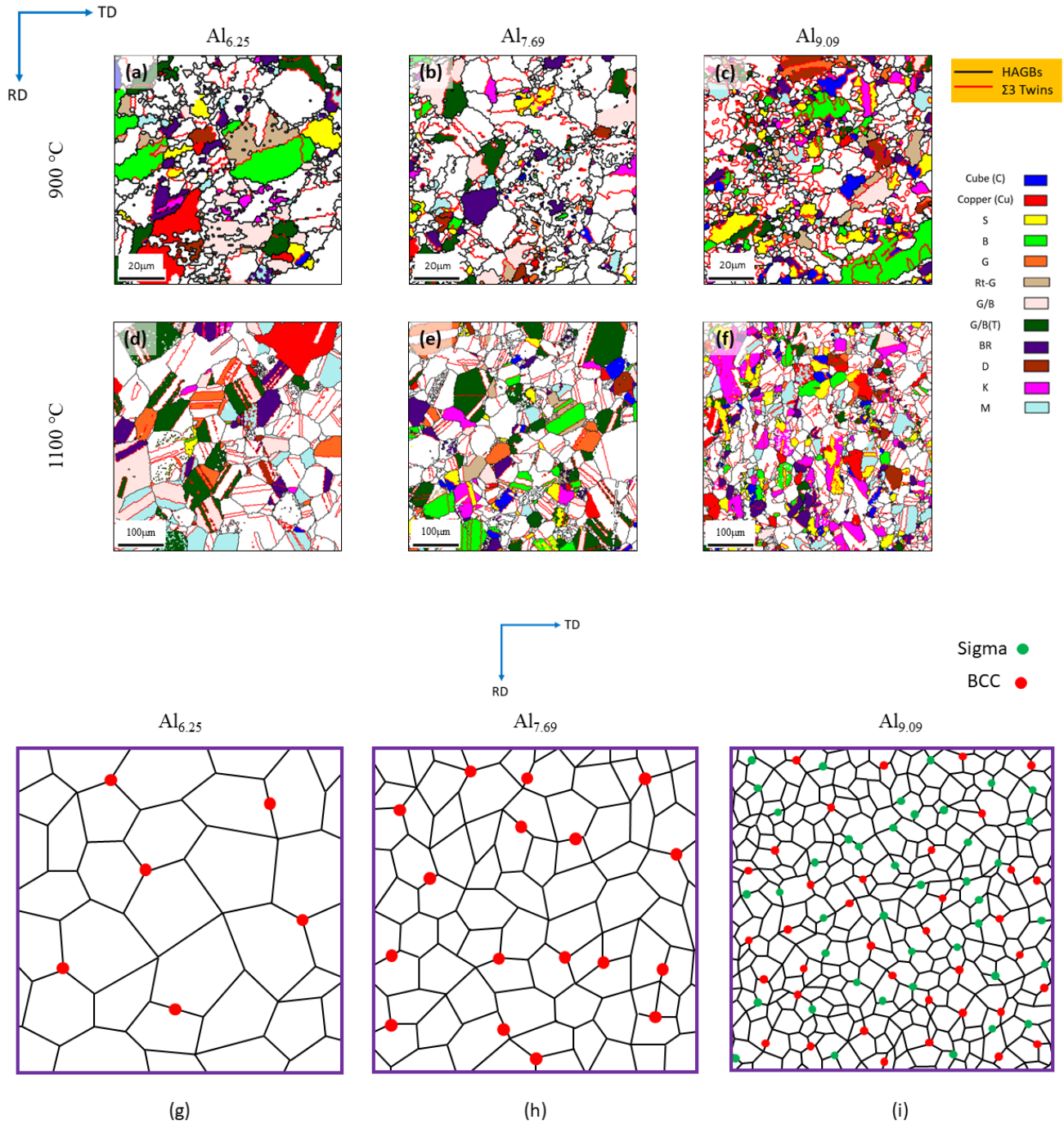

Fig. 7: Orientation maps (OMs) of $Al_{6.25}$ (a, d) $Al_{7.69}$ (b, e) and $Al_{9.09}$ (c, f) MEAs after annealing at 900 °C (a-c) and 1100 °C (d-f). Schematic diagrams are presented for 900 °C annealed $Al_{6.25}$ (g) $Al_{7.69}$ (h) and $Al_{9.09}$ (i) MEAs.

Fig. 8 demonstrates the different microstructural features. The grain size varying with the annealing temperatures, as plotted in Fig. 8(a), clearly indicates the grain growth irrespective of the sample compositions. However, $Al_{9.09}$ MEA consistently shows the presence of finer grains in the material, even at the higher annealing temperature. The grain size profiles, including annealing twins, also show a similar trend. The grain sizes, calculated excluding the annealing twins, of $Al_{9.09}$ MEA are comparatively small and comparable to those of $Al_{6.25}$ and $Al_{7.69}$, which are evaluated, including the annealing twins. The misorientation angle distribution profiles (Fig. 8(b)) of the annealed materials exhibit a very sharp peak near ~60°, implying the development of twins upon annealing treatment. The higher fraction of the annealing twin boundaries (TBs) develops at the higher annealing temperature (1100 °C). However, the fraction of TBs gradually decreases with the increase of the Al content at 1100 °C.

Fig. 8(c, d) reveals the variation of the grain boundary characteristic distribution (GBCD) with the different annealing temperatures at 900 and 1100 °C. At 900 °C (Fig. 8(c)), the increase of Al content reduces the HAGB fraction, although the rate is not too high. Similarly, the increase of the Al content slightly increases the TB fraction. However, the relative difference in the increment could be negligible. Fig. 8(d) explicitly shows the effect of annealing treatment at 1100 °C, where the HAGB fraction increases gradually, while the fraction of TB decreases with the increase of Al-content at 1100 °C. The TB fraction always stays low at lower annealing temperatures irrespective of the alloy compositions compared to higher temperatures. The misorientation angle distribution profiles (Fig. 8(b)) can also corroborate this observation.

The development of the annealing texture is described in Fig. 9(a-c) (after annealing at 900 °C) and Fig. 9(d-f) (after annealing at 1100 °C) for the different Al-containing MEAs after annealing in different temperatures. The $\varphi_2 = 0°$ section of ODF of $Al_{6.25}$ MEA annealed at 900 °C in Fig. 9(a) shows the presence of different texture components with relatively weak

intensities along the α-fiber (sum of B, G, G/B, G/B(T) and Rt-G texture components, ND//<110>). Similarly, weak intensities of the different orientations along the α-fiber can be easily noticed for the other alloy compositions as well after annealing at 900 °C (Fig. 9(b) for $Al_{7.69}$ and Fig. 9(c) for $Al_{9.09}$ MEAs). At the φ_2 = 45° sections (Fig. 9(a) ($Al_{6.25}$), Fig. 9(b) ($Al_{7.69}$) and Fig. 9(c) ($Al_{9.09}$)), the Cu component is either present with weak intensity (Fig. 9(a)) or completely absent (Fig. 9(b, c)). On the other hand, the S component is nearly missing in all the φ_2 = 65° sections of ODFs. The φ_2 = 35° and 45° sections indicate the absence of any perceptible amount of BR and D components, which form the important texture components during recrystallization in low stacking fault energy (SFE) materials. The OMs (Fig. 7(a-c)) also confirm these observations, demonstrating that these components are hardly present. Therefore, overall, it can be stated that the texture development after recrystallization is reasonably weak as more randomly oriented grains become visible (Fig. 7(a-c)). The textural evolution of the materials that have been annealed at a higher temperature (1100 °C) reveals a similar tendency (Fig. 9(d-f)), which can also be corroborated by the OMs (Fig. 7(d-f)).

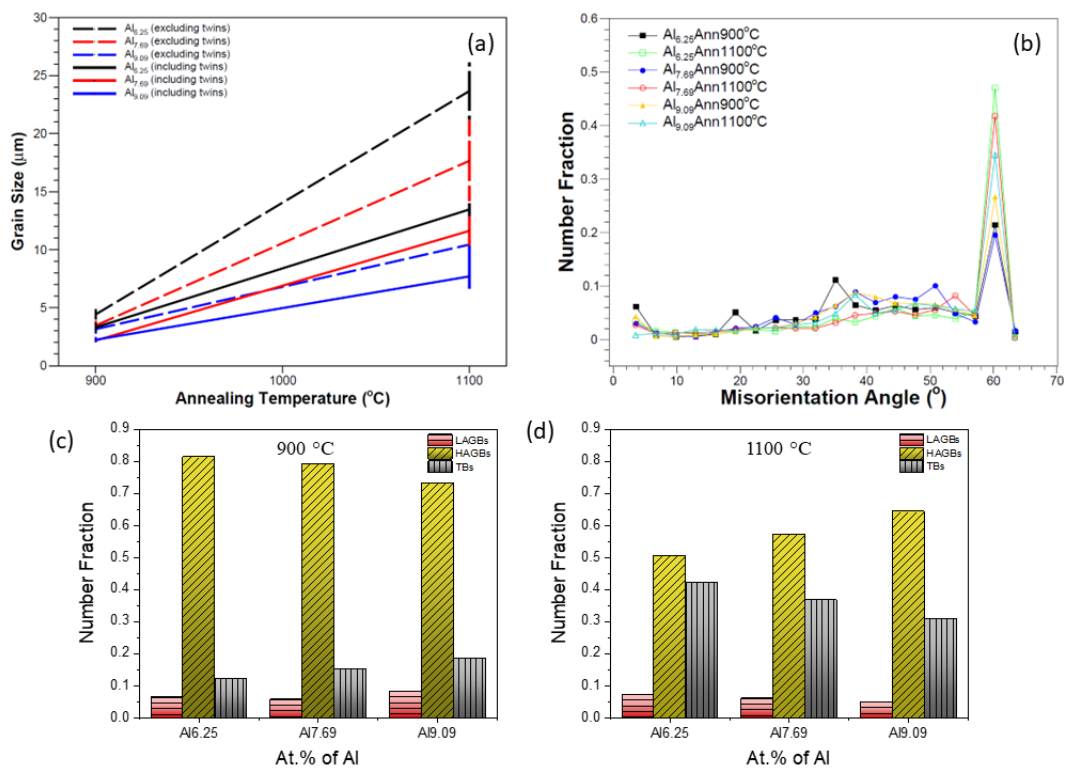

Fig. 8: (a) Variation of grain size with annealing temperature. (b) Misorientation angle distribution of annealed Al-content MEAs. Grain boundary characteristics distribution (GBCD) of (c) 900 °C and (d) 1100 °C annealed Al-content MEAs.

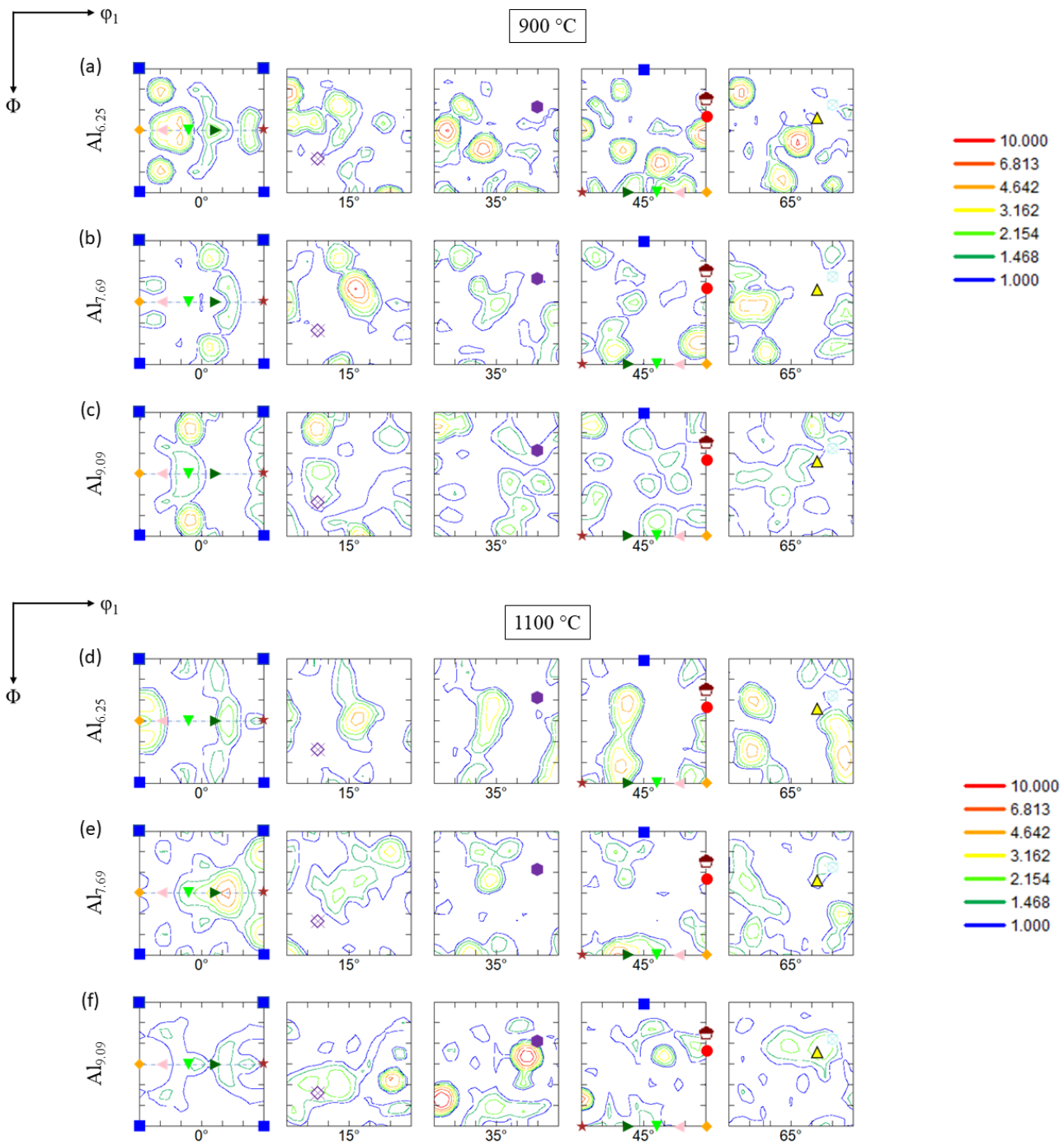

Fig. 9: Selected ODF sections of $Al_{6.25}$ (a, d), $Al_{7.69}$ (b, e), and $Al_{9.09}$ (c, f) MEAs after annealing at 900 °C (a-c) and 1100 °C (d-f). The legends are shown in Table 2.

Fig. 10 illustrates the quantitative assessment of texture development upon annealing for the different Al-containing MEAs. Minor variations (within ~0 – 10%) in the volume fractions of the texture components can be noticed with increasing annealing temperatures. Along with the volume fractions of the texture components of the materials, the variations of the volume fractions of the α-fiber and the random components with the temperatures are also represented graphically. Nominal changes can be seen in the volume fractions of the α-fiber and random components with varying temperatures for $Al_{6.25}$ and $Al_{9.09}$ MEAs. However, the volume fraction of the α-fiber increases slightly after annealing at 1100 °C in $Al_{7.69}$ MEA (Fig. 10(b)). Furthermore, the volume fractions of the random components are always high, irrespective of the compositions and temperatures.

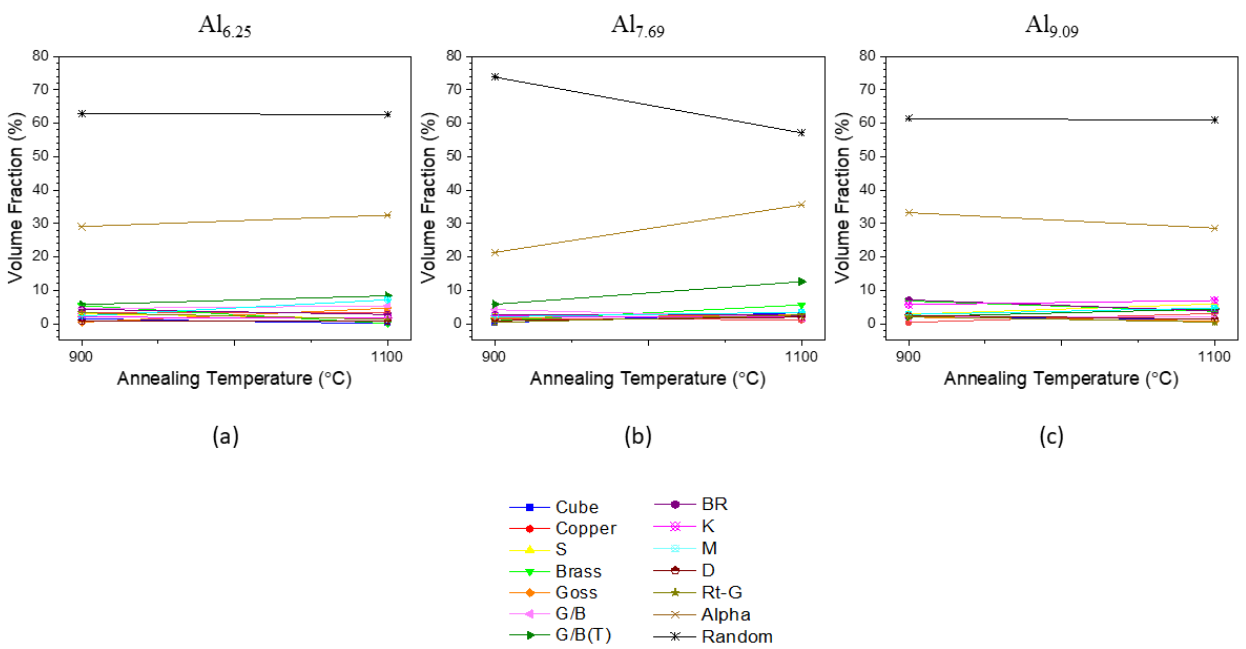

Fig. 10: Variation of volume fraction of different texture components with annealing temperatures for $Al_{6.25}$ (a), $Al_{7.69}$ (b), and $Al_{9.09}$ (c) MEAs.

3.5 Mechanical properties

A well-constructed comparison of the microhardness of the as-cast, deformed, and annealed samples is presented in Fig. 11(a). The Al_x-MEA specimens in as-cast condition show hardness in the range of 185-214 H_v; however, the Al_0 (or CoCrNi) MEA (red dotted line) showed the lowest hardness (~178 H_v). A sharp increase in the hardness of the specimens occurs after heavy deformation. The hardness values (>500 H_v) increase with the increment of the Al-concentration for the deformed samples, similar to the phenomenon observed in the case of the as-cast alloys. The $Al_{9.09}$ MEA shows the highest hardness (~560 H_v) among all the deformed samples. The annealing causes a decrease in the hardness for all the samples. However, the hardness after a lower annealing temperature (700 °C) is quite high compared to other annealed specimens (≥ 450 H_v). The hardness of the $Al_{9.09}$ MEA after annealing at 700 °C (~536 H_v) is comparable to its deformed condition. However, the hardness decreases further with the increase in the annealing temperature due to the significant grain growth at higher annealing temperatures. The hardness values range from 250-350 H_v after annealing at 900 °C, whereas the values decrease further and vary between 205-230 H_v for the samples annealed at 1100 °C. After annealing at 900 °C, $Al_{9.09}$ MEA still exhibits a reasonably high hardness value of ~350 H_v. Although the hardness of the annealed materials decreases with the increase in temperatures, the higher Al-content ($Al_{9.09}$) MEAs consistently show greater hardness at each annealing temperature.

To better comprehend the evolution of the hardness of the different materials at different temperatures, the Hall-Petch relationship is plotted in Fig. 11(b). The relationships are formulated in 2 different ways: (i) considering the empirical relationship of the yield strength and hardness ($\sigma_{YS} = {}^{1}/_{3}\, H_v$ (converted into MPa, 1 H_v = 9.807 MPa)) [46-49] (blue line), and (ii) using the hardness data obtained at different annealing temperatures (red line). According to the empirical relationship between yield strength and hardness, the lattice friction stress and

Hall-Petch coefficient parameters are 438 ± 75 MPa (σ_0) and 1028 ± 140 MPa.$\mu m^{1/2}$ (K), respectively, represented by the blue line. However, based on the hardness data, the parameters are calculated as 134 ± 23 H_v (H_0) and 314 ± 43 $H_v.\mu m^{1/2}$ (K_H), respectively, represented by the red line. The relationship considers only grain size, i.e., excluding twins.

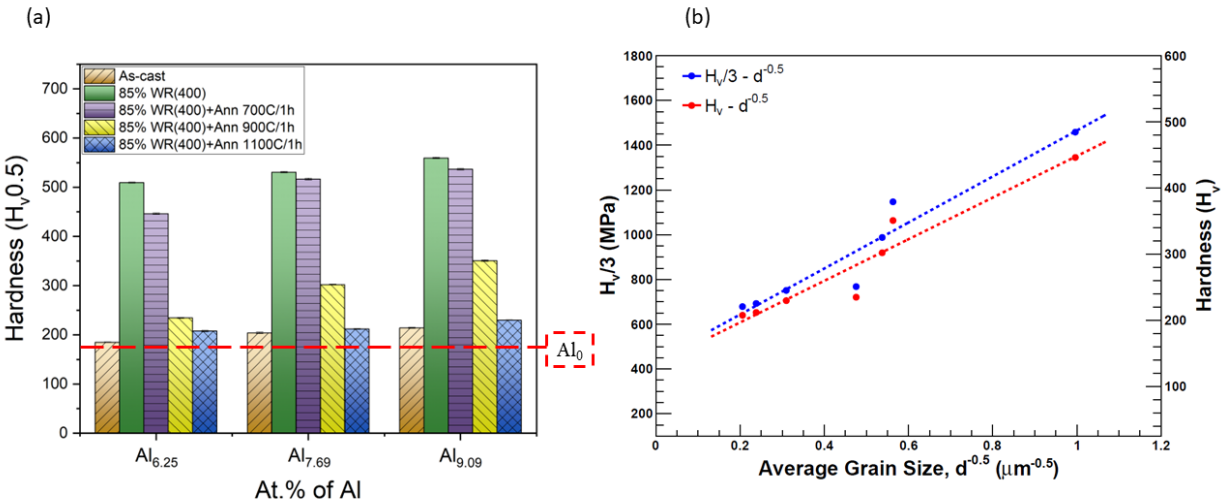

Fig. 11: (a) Hardness profile of as-cast, deformed, and annealed $Al_xCoCrNi$ MEAs. The red dashed line indicates the hardness of as-cast CoCrNi MEA (Al_0). (b) Hall-Petch relationship of $Al_xCoCrNi$ MEAs constructed using hardness (H_v, red line) and yield strength (H_v/3, blue line).

4. **Discussion**

4.1 Microstructure and texture evolution during severe warm-rolling

The present study of severe warm-rolling of different Al-content MEAs leads to the development of ultrafine microstructure with the presence of elongated lamellar structure along RD and deformation inhomogeneities, such as intersecting shear bands and deformation nano-twins. During severe deformation, the materials are subdivided by an enormous number of grain boundaries. The warm-rolling process of these MEAs involves the dynamic transformation of coarser initial grains to an ultrafine deformed structure, which is attributed to the subdivision of the grains. This grain subdivision process involves mechanisms based on the microstructure and texture development for the origin of the high-angle grain boundaries

(HAGBs) after the severe deformation process [50]. The microstructural evolution begins with the cell or substructure formation at the initial stage of deformation by generating low-angle grain boundaries (LAGBs). In the next stage, the dislocations are densified at the LAGBs or triple junctions with further deformation. Finally, following higher deformation, the LAGBs merge to form the HAGBs [50]. Furthermore, the observed textural changes involve the rotation of the different grains to their preferred end orientations by different slip systems [50]. Hence, the severe plastic deformation leading to microstructural and microtextural changes involves the generation of numerous high-angle grain boundaries (HAGBs), accounting for observed ultra-fine structures. These mechanisms are well established for different processed CoCrNi MEA [33, 51].

Notably, the microstructure of the deformed materials contains several deformation heterogeneities, such as shear bands and deformation bands, irrespective of their Al content. The microstructure also reveals the presence of deformation nano-twins, which can be confirmed by the misorientation profile. The development of deformation nano-twins is not unusual for FCC materials with low SFE [31, 51]. However, there are several regions in the microstructure where the misorientation is minimal, suggesting more homogeneous deformation by slipping rather than twinning.

Similar to the microstructural evolution during deformation, SFE plays a significant role in developing the texture during deformation. After cold-rolling, any low SFE FCC metals and alloys can develop brass-type deformation texture with the presence of the B component with relatively higher intensities [52]. The emergence of excessive deformation nano-twins and shear bands during cold-rolling is thought to play a critical role in developing a strong brass-type deformation texture. While this mechanism is still debated and controversial [52, 53], more research is required to fully understand it. Strong brass-type deformation texture was previously reported for the equiatomic single-phase (FCC) ternary CoCrNi MEA after cold-rolling [30, 33, 54], which further satisfies its low SFE of 22 ± 4 mJ/m^2 [21]. In contrast, our

418 present study on Al-containing MEAs shows the presence of the B component is significantly
419 weak after severe warm-rolling, which implies the development of weak brass-type
420 deformation texture. This is very similar in the case of CoCrNi MEA after warm-rolling [31,
421 33]. Such a trend has been observed for the equiatomic quinary CoCrFeMnNi HEA as well,
422 whose calculated SFE is ~20 – 25 mJ/m^2 [55], where a strong brass-type deformation texture
423 developed after cold-rolling [56], while the warm-rolling showed comparatively weaker brass
424 component by developing the pure-metal or copper-type deformation texture [45].

425 The influence of the deformation temperature on SFE has been reported for different alloy
426 systems [57] and single-phase FCC CoCrFeMnNi HEA [58]. Higher SFE reduces the
427 formation of deformation heterogeneities, such as shear bands and deformation nano-twins,
428 and favors more homogeneous deformation. This indicates that the deformation by slipping
429 dominates over the deformation by twinning. Although, in this present investigation, the
430 deformation microstructure shows the development of the shear bands and deformation nano-
431 twins, possibly, the density of the deformation heterogeneities is not adequate to develop the
432 strong brass-type deformation texture.

433 *4.2 Microstructure and texture evolution during recrystallization*

434 Completely recrystallized and fine grains are observed after annealing at 900 °C, while an
435 expected grain growth can be seen after annealing at 1100 °C, irrespective of the Al content. It
436 is noticed that the higher Al-content MEA ($Al_{9.09}$) shows entirely finer grains distributed
437 throughout the microstructure, whereas the mixture of fine and coarse grains is detected in the
438 lower Al-content MEAs ($Al_{6.25}$ and $Al_{7.69}$). Two different mechanisms could be responsible for
439 the presence of finer grains in $Al_{9.09}$ MEA. One of them could be the presence of comparatively
440 higher deformation heterogeneities in $Al_{9.09}$ MEA, which indicates the greater density of the
441 potential nucleation sites compared to the other Al-containing MEAs. The higher hardness of
442 the $Al_{9.09}$ MEA could confirm the possibility of this mechanism. The other possible mechanism

could be the development of the BCC and σ-phases during heat treatment. From the phase analysis (XRD), it is clear that the density of the BCC and σ-phases increases with the increase of the Al-content at a particular annealing temperature. As a result, $Al_{9.09}$ MEA could have more precipitates present after annealing at 700 °C, which may be located either at the grain boundaries or at the triple junction [40]. However, upon annealing at 900 °C, the density of the precipitates could be reduced. This is because the BCC is the only stable phase at 900 °C instead of the σ-phase for $Al_{6.25}$ and $Al_{7.69}$ MEAs. The phase diagram of these alloy systems (Fig.12) can confirm the reduction of the density of the precipitates. On the other hand, the phase diagram suggests that both the precipitates, BCC, and σ-phases could potentially form at 900 °C for $Al_{9.09}$ MEA. The development of these precipitates will always hinder the growth of FCC grains (Fig. 7(g-i)). Therefore, the increase in the density of these precipitates will restrict the grain growth extensively, which can be observed in the case of the $Al_{9.09}$ MEA and confirmed by its higher hardness compared to the other MEAs. However, this mechanism needs further investigation.

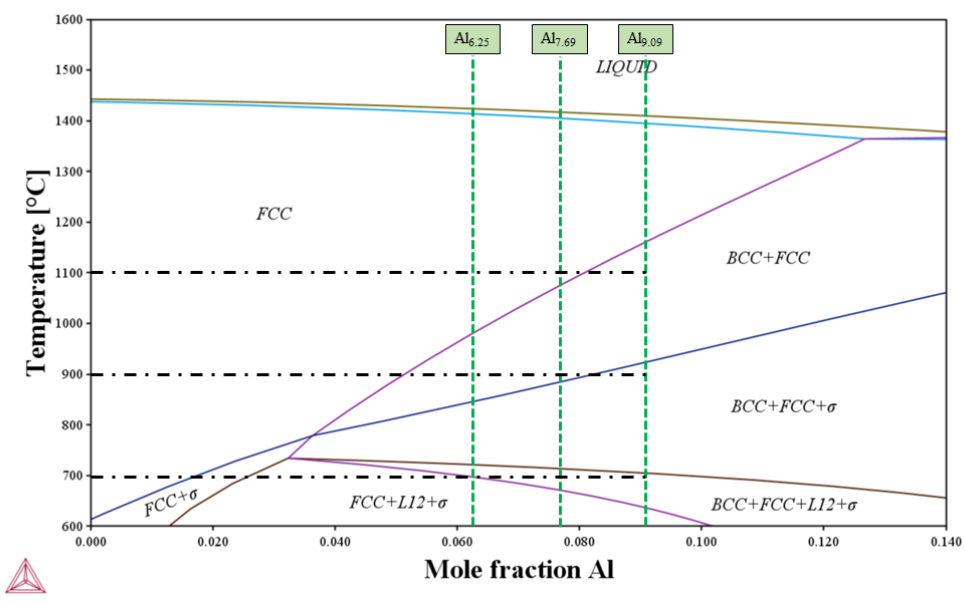

Fig.12: Phase diagram of $Al_xCoCrNi$ MEAs constructed using ThermoCalc software.

The grain growth at the higher annealing temperature of 1100 °C is acceptable and inevitable. The most salient feature is the grain growth behavior of the different Al-containing MEAs at the higher annealing temperature. It is expected from the earlier explanations that $Al_{9.09}$ MEA should have a finer structure even at the higher annealing temperature, which indicates that the grain growth is restricted in this alloy. However, the absolute difference in the grain size at different temperatures is understandably less for $Al_{9.09}$ MEA. Interestingly, this alloy contains only the BCC phase as precipitates at 1100 °C, which can be confirmed from the phase diagram. Nevertheless, the phase analyses of the other two alloys at 1100 °C show the presence of the BCC phase with comparatively lesser intensity and completely single-phase FCC according to the phase diagram. Consequently, the lower Al-containing MEAs with reduced density of the BCC precipitates can grow freely; however, in the case of $Al_{9.09}$ MEA, the presence of more BCC phase restricts the growth of the FCC grains, consequently making it harder and stronger at 1100 °C.

A higher fraction of the annealing twin boundaries (TBs) can be observed for all the alloys. As expected, the fraction of the annealing TBs increases at the higher annealing temperature. Fascinatingly, it is seen that the fraction of annealing TBs decreases with the increase of the Al-content of the alloys at 1100 °C, which indicates a higher fraction of the TBs during the grain growth. In addition to the grain growth that takes place in the lower Al-content MEAs, as previously mentioned, the lower Al-content MEA contains more TBs by consuming the HAGBs at the higher annealing temperature. It is well-known that the driving force for grain growth is the reduction in grain boundary energy, and TBs possess remarkably lower grain boundary energy than HAGBs [59]. As a result, for grain growth at the higher annealing temperature and in the lower Al-content MEA, it is favorable to have more annealing twin boundaries at the expense of the HAGBs by reducing the total grain boundary energy.

The annealing texture, featuring the presence of different α-fiber texture components with relatively weak intensities, signifies the retention of the deformation texture components even

after annealing. It has been observed that more randomly oriented grains are present during annealing, which implies the weakening of the recrystallization texture. Interestingly, this feature of the weak recrystallization texture development can also be realized in the low SFE TWIP steels [60, 61], low SFE CoCrFeMnNi HEA [45, 56, 62-66], and even in the low SFE CoCrNi [31-33, 51]. The development of weak recrystallization texture with the retention of the deformation texture components can rule out the preferential nucleation and growth (PN and PG) mechanism. The emergence of the key recrystallization texture components, brass recrystallization (BR, {236}<385>, growth relationship of BR component with B by 40°<111>) and Dilamore (D, {113}<332>) follow the PN and PG mechanism during the annealing [59]. However, the present study shows the BR and D components are very weak, and the deformation components are retained with minor variations in their volume fractions upon annealing.

4.3 Mechanical Properties

The hardness of the alloys shows a similar trend, increasing after deformation and decreasing with the increase of the annealing temperatures. The hardness of the deformed Al-containing MEAs is higher compared to the warm-rolled equiatomic ternary CoCrNi MEA [33]. Furthermore, the hardness of $Al_{9.09}$ MEA is comparable to the cryo-rolled CoCrNi MEA [51]. The hardness evolution trend of these Al-containing MEAs illustrates that the effect of the Al is quite strong as the hardness increases significantly with the increase of the Al concentration in the alloys. This phenomenon indicates the solid solution strengthening effect of the alloys. Upon annealing at a lower temperature (700 °C), the hardness of $Al_{9.09}$ MEA decreases very slightly and is comparable to its deformed condition. Therefore, it can be predicted that the higher Al-containing MEA possesses the precipitation-strengthening effect. Different strengthening mechanisms can be involved in strengthening the alloys, as shown by the equation:

$$\sigma_{ys} = \sigma_{ss} + \sigma_{ps} + \sigma_{gbs} + \sigma_{ds}$$

where σ_{ys} is the yield strength, σ_{ss} is solid solution strengthening, σ_{ps} is precipitation strengthening, σ_{gbs} is grain boundary strengthening, and σ_{ds} is dislocation strengthening.

Since the hardening behavior of annealed materials is being considered here, the σ_{ds} parameter can be neglected. Due to the presence of Al, lattice distortion is observed, which indicates the effect of the solid solution strengthening (σ_{ss}). From the annealed microstructure, phase analyses (XRD), and phase diagram, the presence of the precipitates can be confirmed, which contributes to precipitation strengthening (σ_{ps}). It is evident from the microstructure that the density of the grain boundary increases with the increase of the Al concentration in the alloys, and, therefore, grain boundary strengthening (σ_{gbs}) can also contribute to the strengthening of the alloys. Consequently, the higher hardness during annealing due to the Al-addition to CoCrNi MEA can corroborate the above three strengthening mechanisms (σ_{ss}, σ_{ps}, and σ_{gbs}). However, to understand their contribution individually, further investigation is required. The Young's modulus difference between the elements present in the alloys also affects the hardness. The Young's modulus of Al is quite low (70 GPa) compared to Co (209 GPa), Cr (279 GPa), and Ni (200 GPa), which increases the Young's modulus misfit and results in the increment of the hardness upon addition of Al.

The lattice friction stress (H_0) and Hall-Petch coefficient (K_H) of the Al-containing MEAs based on hardness are close to the reported values on CoCrNi MEA [67]. However, the values are slightly higher, showcasing the hardening effect owing to Al, especially the grain boundary strengthening effect of the alloys. The lattice friction stress, $\sigma_{0,}$ is comparatively much higher than the HEAs or MEAs composed of 3d transition elements, such as Co, Cr, Fe, Mn, and Ni, as the empirical formula is used to obtain the yield strength from the hardness values. However, it can assumed that the high lattice friction stress of Al-containing HEAs is developed from its chemical composition and the atomic radii of the constituent elements. The difference in the

atomic radii of the present alloys creates severe lattice distortion because of the local atomic arrangements of the elements, which, as a result, increases the lattice friction stress abruptly [68]. On the other hand, the locking parameter or Hall-Petch coefficient (K_H) can be affected by several different factors, including the lattice distortion, the stacking fault energy (SFE), and the shear modulus (G). However, as per previous reports, the lattice distortion factor can be ruled out as it showed some discrepancy in the relationship between lattice distortion and K_H, and it needs to be investigated with a large data set of samples. Lowering the SFE can increase K_H, and it can be surmised that in the present study, the alloys possess lower SFE due to the presence of Al (discussed earlier) [67]. The shear modulus (G) and SFE are inversely related, while the relationship between G and K_H is linear [69, 70], indicating that the Al-containing MEAs possess a higher shear modulus with higher K_H. The relationship between the properties is yet to be validated. From these observations, it is quite clear that grain boundary strengthening by effective grain refinement can play a crucial part in the strengthening of these Al-containing MEAs.

5. Conclusion

Al_xCoCrNi MEA (Al_xCoCrNi) with different concentrations of Al were subjected to thermo-mechanical processing by warm rolling at 400 °C to an 85% thickness reduction, followed by annealing at different temperatures to investigate the effect of Al addition on microstructure and texture. Based on the findings, the following key outputs were concluded.

(i) The severe warm-rolling process produces elongated lamellar banded structure, shear bands, and deformation nano-twins, leading to the development of an ultra-fine microstructure.

(ii) A weak brass-type deformation texture develops after high-temperature warm-rolling, which indicates the rise of the stacking fault energy at the elevated temperature due to homogeneous deformation by slipping rather than by twinning.

(iii) Recrystallized grains were observed after annealing, including the precipitation of the BCC and σ-phases along with the FCC matrix. The increase in annealing temperature leads to grain growth, becoming more pronounced in the lower Al-containing MEAs. With the increase of Al-content, the density of the precipitates or other phases also increases. At the higher annealing temperature, the σ-phase becomes unstable and disappears.

(iv) The development of the weaker recrystallization texture upon annealing and the retention of the deformed texture components rule out the preferential nucleation and growth (PN and PG) phenomena.

(v) The hardness of the as-cast alloys increases with the increase of Al-content. After deformation, the hardness becomes very high but decreases with the increase of the annealing temperatures. Irrespective of the processing conditions, $Al_{9.09}$ MEA always shows the highest hardness. The higher lattice friction stress, obtained from the Hall-Petch relationship, indicates the severe lattice distortion effect due to the different concentrations of Al added to the CoCrNi MEA.

Based on the observations above, it is evident that the warm-rolling process does not only influence the single-phase equiatomic MEA but also can play a crucial role in the evolution of microstructure, texture, and significant improvement in the mechanical properties of Al-containing MEAs and can lead to remarkable strength-ductility balance.

Acknowledgment

The authors acknowledge Mr. Kazuhiko Iida, Mr. Masaki Kobayashi, and Mr. Satoshi Iwasaki from the National Institute for Materials Science (NIMS), Japan, for performing the rolling process used in the current research work.

References

[1] B. Cantor, I.T.H. Chang, P. Knight, A.J.B. Vincent, Microstructural development in equiatomic multicomponent alloys, Mater. Sci. Eng., A 375-377 (2004) 213-218.

[2] J.W. Yeh, S.K. Chen, S.J. Lin, J.Y. Gan, T.S. Chin, T.T. Shun, C.H. Tsau, S.Y. Chang, Nanostructured high-entropy alloys with multiple principal elements: novel alloy design concepts and outcomes, Adv. Eng. Mater. 6(5) (2004) 299–303.

[3] Y.J. Zhao, J.W. Qiao, S.G. Ma, M.C. Gao, H.J. Yang, M.W. Chen, Y. Zhan, A hexagonal close-packed high-entropy alloy: The effect of entropy, Mater. Des. 96 (2016) 10-15.

[4] A. Takeuchi, K. Amiya, T. Wada, K. Yubuta, W. Zhang, High-entropy alloys with a hexagonal close-packed structure designed by equi-atomic alloy strategy and binary phase diagrams, JOM 66(10) (2014) 1984-1992.

[5] M. Feuerbacher, M. Heidelmann, C. Thomas, Hexagonal High-entropy Alloys, Mater. Res. Lett. 3(1) (2015) 1-6.

[6] Y. Yamabe-Mitarai, K. Yanao, Y. Toda, I. Ohnuma, T. Matsunaga, Phase stability of Ti-containing high-entropy alloys with a bcc or hcp structure, J. Alloys Compd. 911 (2022) 164849.

[7] O.N. Senkov, G.B. Wilks, D.B. Miracle, C.P. Chuang, P.K. Liaw, Refractory high-entropy alloys, Intermetallics 18(9) (2010) 1758-1765.

[8] Y.F. Ye, Q. Wang, J. Lu, C.T. Liu, Y. Yang, High-entropy alloy: challenges and prospects, Mater. Today 19(6) (2016) 349-362.

[9] M.H. Tsai, J.W. Yeh, High-entropy alloys: a critical review, Math. Res. Lett. 2(3) (2014) 107–123.

[10] J.W. Yeh, Recent progress in high-entropy alloys, Ann. Chim. Sci. Mat. 31(6) (2006) 633-648.

[11] B. Cantor, Multicomponent and High Entropy Alloys, Entropy 16(9) (2014) 4749-4768.

[12] B.S. Murty, J.W. Yeh, S. Ranganathan, P.P. Bhattacharjee, High-entropy alloys, second ed., Elsevier, 2019.

[13] J. Yeh, Y. Chen, S.-J. Lin, S.-K. Chen, High-Entropy Alloys – A New Era of Exploitation Mater. Sci. Forum 560 (2007) 1-9.

[14] Y. Zhang, T.T. Zuo, Z. Tang, M.C. Gao, K.A. Dahmen, P.K. Liaw, Z.P. Lu, Microstructures and properties of high-entropy alloys, Prog. Mater. Sci. 61 (2014) 1–93.

[15] D.B. Miracle, O.N. Senkov, A critical review of high entropy alloys and related concepts, Acta Mater. 122 (2017) 448-511.

[16] D.B. Miracle, J.D. Miller, O.N. Senkov, C. Woodward, M.D. Uchic, J. Tiley, Exploration and Development of High Entropy Alloys for Structural Applications, Entropy 16(1) (2014) 494-525.

[17] E.P. George, W.A. Curtin, C.C. Tasan, High entropy alloys: a focused review of mechanical properties and deformation mechanisms, Acta Mater. 188 (2020) 435–474.

[18] D.B. Miracle, High entropy alloys as a bold step forward in alloy development, Nat. Commun. 10(1) (2019) 1805.

[19] J.W. Yeh, S.J. Lin, Breakthrough applications of high-entropy materials, J. Mater. Res. 33(19) (2018) 3129 - 3137.

[20] E.P. George, D. Raabe, R.O. Ritchie, High-entropy alloys, Nat. Rev. Mater. 4(8) (2019) 515–534.

[21] G. Laplanche, A. Kostka, C. Reinhart, J. Hunfeld, G. Eggeler, E.P. George, Reasons for the superior mechanical properties of medium-entropy CrCoNi compared to high-entropy CrMnFeCoNi, Acta Mater. 128 (2017) 292-303.

[22] B. Gludovatz, A. Hohenwarter, K.V. S. Thurston, H. Bei, Z. Wu, E.P. George, R.O. Ritchie, Exceptional damage-tolerance of a medium-entropy alloy CrCoNi at cryogenic temperatures, Nat. Commun. 7 (2016) 10602.

[23] C.E. Slone, J. Miao, E.P. George, M.J. Mills, Achieving ultra-high strength and ductility in equiatomic CrCoNi with partially recrystallized microstructures, Acta Mater. 165 (2019) 496-507.
[24] H.W. Deng, Z.M. Xie, B.L. Zhao, Y.K. Wang, M.M. Wang, J.F. Yang, T. Zhang, Y. Xiong, X.P. Wang, Q.F. Fang, C.S. Liu, Tailoring mechanical properties of a CoCrNi medium-entropy alloy by controlling nanotwin-HCP lamellae and annealing twins, Mater. Sci. Eng., A 744 (2019) 241-246.
[25] J. Ding, Q. Yu, M. Asta, R.O. Ritchie, Tunable stacking fault energies by tailoring local chemical order in CrCoNi medium-entropy alloys, PNAS 115(36) (2018) 8919-8924.
[26] C.E. Slone, S. Chakraborty, J. Miao, E.P. George, M.J. Mills, S.R. Niezgoda, Influence of deformation induced nanoscale twinning and FCC-HCP transformation on hardening and texture development in medium-entropy CrCoNi alloy, Acta Mater. 158 (2018) 38-52.
[27] Z. Wu, H. Bei, F. Otto, G.M. Pharr, E.P. George, Recovery, recrystallization, grain growth and phase stability of a family of FCC-structured multi-component equiatomic solid solution alloys, Intermetallics 46 (2014) 131-140.
[28] Z. Wu, H. Bei, G.M. Pharr, E.P. George, Temperature dependence of the mechanical properties of equiatomic solid solution alloys with face-centered cubic crystal structures, Acta Mater. 81 (2014) 428 – 441.
[29] P. Sathiyamoorthi, J.W. Bae, P. Asghari-Rad, J.M. Park, J.G. Kim, H.S. Kim, Effect of annealing on microstructure and tensile behavior of CoCrNi medium entropy alloy processed by high-pressure torsion. Entropy 20(11) (2018) 849.
[30] G.D. Sathiaraj, W. Skrotzki, A. Pukenas, R. Schaarschuch, R.J. Immanuel, S.K. Panigrahi, J.A. Chelvane, S.S.S. Kumar, Effect of annealing on the microstructure and texture of cold rolled CrCoNi medium-entropy alloy, Intermetallics 101 (2018) 87-98.
[31] J. Saha, R. Saha, P.P. Bhattacharjee, Microstructure and texture of severely warm-rolled and annealed coarse-grained CoCrNi medium entropy alloy (MEA): A perspective on the initial grain size effect, J. Alloys Compd. 904 (2022) 163954.
[32] J. Saha, R. Saha, P.P. Bhattacharjee, Microstructure and texture development in CoCrNi medium entropy alloy processed by severe warm cross-rolling and annealing, Intermetallics 143 (2022) 107463.
[33] J. Saha, P. Bhattacharjee, Influences of Thermomechanical Processing by Severe Cold and Warm Rolling on the Microstructure, Texture, and Mechanical Properties of an Equiatomic CoCrNi Medium-Entropy Alloy, J. Mater. Eng. Perf. (2021) 1-16.
[34] T.S. Reddy, I.S. Wani, T. Bhattacharjee, S.R. Reddy, R. Saha, P.P. Bhattacharjee, Severe plastic deformation driven nanostructure and phase evolution in a $Al_{0.5}$CoCrFeMnNi dual phase high entropy alloy, Intermetallics 91 (2017) 150-157.
[35] I.S. Wani, G. D. Sathiaraj, M.Z. Ahmed, S.R. Reddy, P.P. Bhattacharjee, Evolution of microstructure and texture during thermo-mechanical processing of a two phase $Al_{0.5}$CoCrFeMnNi high entropy alloy, Mater. Charact. 118 (2016) 417-424.
[36] C.-J. Tong, M.-R. Chen, J.-W. Yeh, S.-J. Lin, S.-K. Chen, T.-T. Shun, S.-Y. Chang, Mechanical performance of the Al_xCoCrCuFeNi high-entropy alloy system with multiprincipal elements, Metall. Mater. Trans. A 36(5) (2005) 1263-1271.
[37] Y. Sun, P. Chen, L. Liu, M. Yan, X. Wu, C. Yu, Z. Liu, Local mechanical properties of Al_xCoCrCuFeNi high entropy alloy characterized using nanoindentation, Intermetallics 93 (2018) 85-88.
[38] C.-W. Tsai, Y.-L. Chen, M.-H. Tsai, J.-W. Yeh, T.-T. Shun, S.-K. Chen, Deformation and annealing behaviors of high-entropy alloy $Al_{0.5}$CoCrCuFeNi, J. Alloys Compd. 486(1) (2009) 427-435.

[39] D. Lee, H.-U. Jeong, K.-H. Lee, J.B. Jeon, N. Park, Precipitation and grain-boundary strengthening of Al-added CoCrNi medium-entropy alloys, Mater. Lett. 250 (2019) 127-130.
[40] P. Sathiyamoorthi, P.J. Min, M. Jongun, J.W. Bae, P. Asghari-Rad, A. Zargaran, H.S. Kim, Achieving high strength and high ductility in $Al_{0.3}$CoCrNi medium-entropy alloy through multi-phase hierarchical microstructure, Materialia 8 (2019) 100442.
[41] M.P. Agustianingrum, S. Yoshida, N. Tsuji, N. Park, Effect of aluminum addition on solid solution strengthening in CoCrNi medium-entropy alloy, J. Alloys Compd. 781 (2019) 866-872.
[42] D. Lee, M.P. Agustianingrum, N. Park, N. Tsuji, Synergistic effect by Al addition in improving mechanical performance of CoCrNi medium-entropy alloy, J. Alloys Compd. 800 (2019) 372-378.
[43] W. Lu, X. Luo, Y. Yang, J. Zhang, B. Huang, Effects of Al addition on structural evolution and mechanical properties of the CrCoNi medium-entropy alloy, Mater. Chem. Phys. 238 (2019) 121841.
[44] S.R. Reddy, S. Yoshida, U. Sunkari, A. Lozinko, J. Joseph, R. Saha, D. Fabijanic, S. Guo, P.P. Bhattacharjee, N. Tsuji, Engineering heterogeneous microstructure by severe warm-rolling for enhancing strength-ductility synergy in eutectic high entropy alloys, Mater. Sci. Eng., A 764 (2019) 138226.
[45] J. Saha, G. Ummethala, S.R.K. Malladi, P.P. Bhattacharjee, Severe warm-rolling mediated microstructure and texture of equiatomic CoCrFeMnNi high entropy alloy: A comparison with cold-rolling, Intermetallics 129 (2021) 107029.
[46] C.J. Youngdahl, P.G. Sanders, J.A. Eastman, J.R. Weertman, Compressive yield strengths of nanocrystalline Cu and Pd, Scr. Mater. 37(6) (1997) 809-813.
[47] P.G. Sanders, C.J. Youngdahl, J.R. Weertman, The strength of nanocrystalline metals with and without flaws, Mater. Sci. Eng., A 234-236 (1997) 77-82.
[48] H. Li, F. Ebrahimi, Synthesis and characterization of electrodeposited nanocrystalline nickel–iron alloys, Mater. Sci. Eng., A 347(1) (2003) 93-101.
[49] H.W. Zhang, G. Subhash, X.N. Jing, L.J. Kecskes, R.J. Dowding, Evaluation of hardness–yield strength relationships for bulk metallic glasses, Philos. Mag. Lett. 86(5) (2006) 333-345.
[50] D.A. Hughes, N. Hansen, High angle boundaries formed by grain subdivision mechanisms, Acta Mater. 45(9) (1997) 3871-3886.
[51] J. Saha, R. Saha, S.R.K. Malladi, P.P. Bhattacharjee, Microstructure and texture of CoCrNi medium entropy alloy (MEA) processed by severe cryo-rolling: A study vis-a-vis cold-rolling, Intermetallics 138 (2021) 107345.
[52] T. Leffers, R.K. Ray, The brass-type texture and its deviation from the copper type texture, Prog. Mater. Sci. 54(3) (2009) 351–396.
[53] R. Madhavan, R.K. Ray, S. Suwas, Texture transition in cold-rolled nickel–40wt.% cobalt alloy, Acta Mater. 74 (2014) 151-164.
[54] G.D. Sathiaraj, R. Kalsar, S.S.S. Kumar, S. Suwas, W. Skrotzki, Evolution of texture during cold-rolling of a CrCoNi medium-entropy alloy, Mater. Today:. Proc. 27 (2020) 2147-2151.
[55] A.J. Zaddach, C. Niu, C.C. Koch, D.L. Irving, Mechanical Properties and Stacking Fault Energies of NiFeCrCoMn High-Entropy Alloy, JOM 65(12) (2013) 1780-1789.
[56] G.D. Sathiaraj, P.P. Bhattacharjee, Effect of cold-rolling strain on the evolution of annealing texture of equiatomic CoCrFeMnNi high entropy alloy, Mater. Charact. 109 (2015) 189-197.
[57] P.C.J. Gallagher, The Influence of alloying, temperature, and related effects on the stacking fault energy, Metall. Mater. Trans. B 1(9) (1970) 2429-2461.

[58] S. Huang, W. Li, S. Lu, F. Tian, J. Shen, E. Holmström, L. Vitos, Temperature dependent stacking fault energy of FeCrCoNiMn high entropy alloy, Scr. Mater. 108 (2015) 44-47.
[59] F.J. Humphreys, M. Hatherly, Recrystallization and Related Annealing Phenomena, second ed., Elsevier, Oxford, 2004.
[60] L. Bracke, K. Verbeken, L.A.I. Kestens, J. Penning, Microstructure and texture evolution during cold rolling and annealing of a high Mn TWIP steel, Acta Mater. 57(5) (2009) 1512–1524.
[61] L. Bracke, K. Verbeken, L.A.I. Kestens, Texture generation and implications in TWIP steels, Scr. Mater. 66(12) (2012) 1007–1011.
[62] N. Stepanov, M. Tikhnovsky, N. Yurchenko, D. Zyabkin, M. Klimova, S. Zherebtsov, A.Efimov, G.Salishchev, Effect of cryo-deformation on structure and properties of CoCrFeNiMn high-entropy alloy, Intermetallics 59 (2015) 8–17.
[63] P.P. Bhattacharjee, G.D. Sathiaraj, M. Zaid, J.R. Gatti, C. Lee, C.W. Tsai, J.W. Yeh, Microstructure and texture evolution during annealing of equiatomic CoCrFeMnNi high-entropy alloy, J. Alloys Compd. 587 (2014) 544–552.
[64] G.D. Sathiaraj, P.P. Bhattacharjee, Analysis of microstructure and microtexture during grain growth in low stacking fault energy equiatomic CoCrFeMnNi high entropy and Ni-60 wt.% Co alloys, J. Alloys Compd. 637 (2015) 267–276.
[65] G.D. Sathiaraj, P.P. Bhattacharjee, C.W. Tsai, J.W. Yeh, Effect of heavy cryo-rolling on the evolution of microstructure and texture during annealing of equiatomic CoCrFeMnNi high entropy alloy, Intermetallics 69 (2016) 1-9.
[66] G.D. Sathiaraj, M.Z. Ahmed, P.P. Bhattacharjee, Microstructure and texture of heavily cold-rolled and annealed fcc equiatomic medium to high entropy alloys, J. Alloys Compd. 664 (2016) 109-119.
[67] Y.-C. Huang,C.-H. Su,S.-K. Wu, C. Lin, A Study on the Hall–Petch Relationship and Grain Growth Kinetics in FCC-Structured High/Medium Entropy Alloys, Entropy 21(3) (2019).
[68] S. Yoshidaa, T. Bhattacharjee, Y. Bai, N. Tsuji, Friction stress and Hall-Petch relationship in CoCrNi equi-atomic medium entropy alloy processed by severe plastic deformation and subsequent annealing, Scr. Mater. 134 (2017) 33-36.
[69] I. Moravcik, H. Hadraba, L. Li, I. Dlouhy, D. Raabe, Z. Li, Yield strength increase of a CoCrNi medium entropy alloy by interstitial nitrogen doping at maintained ductility, Scr. Mater. 178 (2020) 391-397.
[70] D. Wu, J. Zhang, J.C. Huang, H. Bei, T.G. Nieh, Grain-boundary strengthening in nanocrystalline chromium and the Hall–Petch coefficient of body-centered cubic metals, Scr. Mater. 68(2) (2013) 118-121.

Declaration of interests

☒The authors declare that they have no known competing financial interests or personal relationships that could have appeared to influence the work reported in this paper.

☐The authors declare the following financial interests/personal relationships which may be considered as potential competing interests: